

Key Points:

- Glaciovolcanism creates large deposits of altered fragmented volcanic glass distinct from subaerial volcanism
- Glaciation can suppress magmatism, driving geochemical and mineralogical diversity in an area once deglaciation starts
- Glaciovolcanism may have occurred on Mars with explosive phreatomagmatic units more likely under Mars' planetary conditions

Supporting Information:

Supporting Information may be found in the online version of this article.

Correspondence to:

C. C. Bedford,
cbedford@purdue.edu

Citation:

Bedford, C. C., Rampe, E. B., Thorpe, M. T., Ewing, R. C., Mason, K., Horgan, B., et al. (2024). The geochemical and mineralogical signature of glaciovolcanism near Þórisjökull, Iceland, and its implications for glaciovolcanism on Mars. *Journal of Geophysical Research: Planets*, 129, e2023JE008261. <https://doi.org/10.1029/2023JE008261>

Received 19 DEC 2023

Accepted 23 JUN 2024

Author Contributions:

Conceptualization: Candice C. Bedford

Funding acquisition: Elizabeth

B. Rampe, Ryan C. Ewing, Briony Horgan, Ewan Reid

Investigation: Candice C. Bedford

Methodology: Candice C. Bedford, Elizabeth B. Rampe, Michael T. Thorpe, Ryan C. Ewing, Kashauna Mason, Briony Horgan, Amanda Rudolph, Mathieu G. A. Lapôtre, Prakhar Sinha, Marion Nachon, Emily Champion, Lauren Berger, Ewan Reid, Patrick C. Gray











Resources: Ryan C. Ewing

Supervision: Elizabeth B. Rampe, Ryan C. Ewing

© 2024. The Author(s).

This is an open access article under the terms of the [Creative Commons Attribution License](https://creativecommons.org/licenses/by/4.0/), which permits use, distribution and reproduction in any medium, provided the original work is properly cited.

The Geochemical and Mineralogical Signature of Glaciovolcanism Near Þórisjökull, Iceland, and Its Implications for Glaciovolcanism on Mars

Candice C. Bedford^{1,2,3} , Elizabeth B. Rampe² , Michael T. Thorpe^{4,5} , Ryan C. Ewing⁶ , Kashauna Mason⁶, Briony Horgan⁷ , Amanda Rudolph⁷ , Mathieu G. A. Lapôtre⁸ , Prakhar Sinha⁷, Marion Nachon⁶ , Emily Champion⁶, Lauren Berger⁶ , Ewan Reid⁹, and Patrick C. Gray¹⁰ 

¹Lunar and Planetary Institute, Universities Space Research Association, Houston, TX, USA, ²Astromaterials Research and Exploration Science Division, NASA Johnson Space Center, Houston, TX, USA, ³Now at Department of Earth, Atmospheric, and Planetary Sciences, Purdue University, West Lafayette, IN, USA, ⁴University of Maryland, College Park, MD, USA, ⁵NASA Goddard Space Flight Center, Greenbelt, MD, USA, ⁶Texas A&M University, College Station, TX, USA, ⁷Purdue University, West Lafayette, IN, USA, ⁸Department of Earth and Planetary Sciences, Stanford University, Stanford, CA, USA, ⁹Mission Control Space Services Ltd., Ottawa, ON, Canada, ¹⁰Duke University, Durham, NC, USA

Abstract Candidate glaciovolcanic landforms have been identified across Mars, suggesting that volcano-ice interactions may have been relatively widespread in areas that once contained extensive surface and near-surface ice deposits. To better constrain the detection of glaciovolcanism in Mars' geological record, this study has investigated and characterized the petrology, geochemistry, and mineralogy of three intraglacial volcanoes and an interglacial volcano in the Þórisjökull area of southwest Iceland. Our results show that glaciovolcanism creates abundant, variably altered hyaloclastite and hyalotuff that is sufficiently geochemically and mineralogically distinctive from subaerially erupted lava for identification using instruments available on Mars rovers and landers. Due to the lower gravity and atmospheric pressure at the surface of Mars, hyaloclastite and hyalotuff are also more likely to form in greater abundance in Martian glaciovolcanoes. Our results support that magmatism following deglaciation likely triggers decompression melting of the shallow mantle beneath Iceland, creating systematic changes in geochemistry and mineralogy. Glaciation can also suppress magmatism at its peak, encouraging the formation of shallow fractionated magma chambers. As such, it is possible for the crustal loading of an ice cap to enhance igneous diversity on a planet without plate tectonism, creating glass-rich, altered, and mineralogically diverse deposits such as those discovered in Gale crater by the Curiosity rover. However, as the eroded products of glaciovolcanism are similar to those formed through hydrovolcanism, the presence of a glaciovolcanic landform at the source is required to confirm whether volcano-ice interactions occurred at the sediment source.

Plain Language Summary The ancient Martian climate has been long debated with scientists hypothesizing that the river channels and lake beds preserved on the surface today formed in either a warm and wet environment or a cold and icy environment, with heating events driving large-scale melting. One such heating event includes volcanism. This study investigated the chemical and mineralogical impact of volcano-ice interactions in Iceland using techniques available to Mars rovers and landers to improve the detection of these deposits on Mars. Our results show that deposits rich in glass and the early products of low temperature alteration (palagonite, clays, zeolites) are likely to be more prevalent on Mars compared to the Earth due to differences in gravity between the two planets. Furthermore, the presence of a thick ice cap on Mars may encourage a diversity of lava compositions to form in shallow magma chambers as the weight of a thick ice cap can suppress volcanism. These types of deposits are identifiable using Mars rover and lander techniques, but due to their similarities to other volcanic units that may have erupted in the presence of water, a candidate glaciovolcanic landform is needed to confirm that these deposits are from volcano-ice interactions.

1. Introduction

Mars' surface displays evidence of widespread surface water in its ancient past (>3 Ga), forming features such as inverted fluvial deposits (Davis et al., 2016; Dickson et al., 2021; Weitz et al., 2008), deltas (Fassett &

Writing – original draft: Candice

C. Bedford

Writing – review & editing: Candice

C. Bedford, Elizabeth B. Rampe, Michael

T. Thorpe, Amanda Rudolph, Mathieu

G. A. Lapôtre

Head, 2005; Morgan et al., 2022; Ori et al., 2000; Schon et al., 2012), crater lakes (Bhattacharya et al., 2005; Grotzinger et al., 2014; Newsom et al., 1996; Thomson et al., 2011; N. Warner et al., 2010), and potentially oceans (Baker et al., 1991; M. Carr & Head, 2019; Clifford & Parker, 2001; Di Achille & Hynes, 2010; Parker et al., 1993; Xiao et al., 2023). A transition in mineralogy from phyllosilicates to sulfates to anhydrous minerals is also detected from orbit, indicating a diminishing water supply over geological time (Bibring et al., 2005; Ehlmann & Edwards, 2014; Mustard et al., 2008). However, there has been a long-standing debate as to whether this geomorphological and mineralogical evidence indicates a warmer and wetter Mars (Craddock & Howard, 2002; Craddock & Maxwell, 1993) or whether the surface water only transiently flowed during episodic warming events, for example, triggered by impacts or volcanism on an ice-covered world (Bishop et al., 2018; Head & Wilson, 2007; Squyres & Kasting, 1994; Wordsworth et al., 2021). Searching for signs of ice throughout Mars' geologic record can aid in constraining Mars' ancient climate and improve our understanding of surface processes and habitability on early Mars.

Many paleoclimate studies on Mars revolve around investigating and explaining the planet's sedimentary record, but the volcanic source rocks of the sediments can themselves be a paleoclimate indicator (e.g., Smellie et al., 2008) and affect the characteristics of the eroded sediments. On the Earth, distinctive volcanic landforms form when an eruption occurs in the presence of a thick ice cap (Figure 1). This type of glaciovolcanic eruption results in steep sided mounds of pillow, hyaloclastite (including pillow breccia), and hyalotuff and can be capped by a flat top of subaerial lava flows. Glaciovolcanic mounds can be linear (tindars), circular (tuyas), or exist as a sheet of pillow basalt (móberg sheets) (Jakobsson & Gudmundsson, 2008; Pedersen et al., 2020). As a result, glaciovolcanic landforms stand out in comparison to the smoother, low angled slopes of shield volcanoes or the cinder cones that can otherwise form as a result of subaerial basaltic eruptions on the Earth or Mars (Figure 1).

Several candidate glaciovolcanic landforms have been identified on Mars from orbital data, including tuyas, tindars, and móberg sheets (C. Allen, 1979; Chapman, 1994; Chapman & Tanaka, 2002; Ghatan & Head, 2002; Hodges & Moore, 1979; Kadish et al., 2008; Martínez-Alonso et al., 2011; Scanlon et al., 2014). These are largely restricted to Amazonian terrain within the northern lowlands of Mars such as Acidalia Planitia and Chryse Planitia (C. Allen, 1979; Martínez-Alonso et al., 2011) or on the slopes of Tharsis volcanoes (Hodges & Moore, 1979; Kadish et al., 2008; Scanlon et al., 2014), but some studies have also identified potential tuyas and other subglacial volcanic landforms on Hesperian-aged terrain around the south polar ice cap (Ghatan & Head, 2002) and Valles Marineris (Chapman & Tanaka, 2002) (Figure 2). One of the oldest geomorphological features on Mars hypothesized to have a glaciovolcanic origin is the 6-km-high escarpment with extensive lobate aureoles at its base on Olympus Mons, potentially placing the subglacial eruptive period in the Noachian (Hodges & Moore, 1979). Subterranean volcano-ice interactions have also been hypothesized for Mars due to the likely presence of extensive ground ice deposits. Candidate volcano-ground ice interaction features have included the chasmata, chaos, and surface materials of Xanthe, Margaritifer, and Meridiani Terrae (Chapman & Tanaka, 2002; Head & Wilson, 2007). Detecting geomorphological evidence of glaciovolcanism on Noachian and Hesperian Mars terrain is difficult as most candidate glaciovolcanic landforms are susceptible to erosion because they are predominantly derived from hyaloclastite or hyalotuff materials (Jakobsson & Gudmundsson, 2008; Martínez-Alonso et al., 2011). Older glaciovolcanic landforms can also become mantled with extensive regolith and dust deposits (Martínez-Alonso et al., 2011). There is thus a need for a thorough characterization of the geochemical and petrological characteristics of glaciovolcanic materials to aid in their identification throughout the geological record, particularly for landed Mars missions that explore geological units with a variety of geochemical and mineralogical techniques at different analytical scales.

NASA missions sent to the surface of Mars have aimed to investigate the planet's geological history and its potential for life. As such, most missions have been sent to sedimentary basins such as the Curiosity rover in Gale crater and Perseverance rover in Jezero crater in an effort to “follow the water” with the understanding that on Earth, where there is water, there is the potential for life. With most missions going to sedimentary basins, it is critical to understand and constrain source-to-sink processes so that information regarding Mars surface processes (e.g., as volcanic eruptions) and climate can be extracted (McLennan et al., 2019). Source-to-sink studies on the Earth have been extensive, however, the vast majority of these have investigated continental crust which has a different geochemistry and mineralogy to the crust of planetary bodies in our solar system (Lapôtre et al., 2022; McLennan et al., 2019). Earth-based source-to-sink studies also benefit from direct access to geological materials under investigation and can utilize microscopic laboratory techniques that are not available to rover and lander missions to Mars. As a result, Mars-analog missions aim to bridge this gap in understanding between planetary

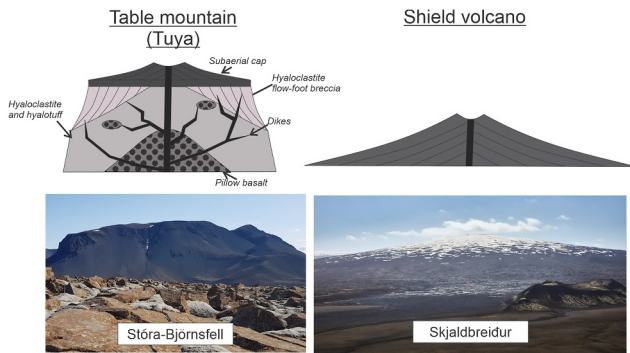


Figure 1. Schematic diagram cross-sections comparing a glaciovolcanic landform known as a Tuya or Table Mountain (a) and its subaerial equivalent, a shield volcano (b) alongside images of these landforms from the SAND-E 2019 field site (c) the Tuya Stóra-Björnsfell, and (d) shield volcano Skjaldbreiður.

systems and the techniques available to a rover and help us to prepare for future Mars sample return with the Mars 2020 mission.

1.1. Glaciovolcanism

Lava morphologies from glaciovolcanism are considered hydrovolcanic deposits and are different from those of effusive, subaerial eruptions that did not encounter water during the eruption. Glaciovolcanic lava morphologies also form in relation to the stage of the eruption and thickness of the overlying ice sheet (Pedersen et al., 2020). In the initial stages of a glaciovolcanic eruption, the propagation of a dike into an overlying ice cap causes a pocket of meltwater to form as an englacial lake at the base of the ice. Pressure from a thick overlying ice cap suppresses volatile release and lava-water interactions during the eruption, creating effusive underwater eruptive products such as pillow basalts or kubbaberg (cube-jointed) lava sheets. During this early, effusive stage, quench-fragmentation and mechanical spalling of lava rinds due to deformation from advancing flow can also create hyaloclastite consisting of poorly vesicular, blocky, coarse, sideromelane and tachylite within

a palagonitic matrix (Smellie, 2008; van Otterloo et al., 2015). As the eruption progresses and the volcanic mound grows, pressure from the overlying ice cap decreases with increasing height of the volcanic mound, increasing the likelihood of explosivity due to fragmentation through volatile release, forming hyalotuff. For this paper, we adopt the classification scheme of Smellie et al. (2008) to differentiate hyaloclastite from hyalotuff. As such, hyalotuff is used to describe variably vesicular deposits that are blocky or cusped in shape, reflecting a more explosive eruptive environment. Both hyaloclastite and hyalotuff deposits can contain brecciated fragments of previous pillow and hyaloclastite deposits within a lapilli to ash matrix that is weakly cemented by the interaction of hot lava with englacial lake water trapped within the pore spaces.

As the eruption continues and the volcanic edifice grows, the overlying ice thins due to melting, causing subsidence of the overlying ice. Eventually, the overlying ice completely melts or collapses to expose the englacial lake. In this phase, explosive phreatomagmatic eruptions can occur, erupting a column containing ash and lapilli. The ash and lapilli in the column are sorted as they settle back to the Earth and those deposits can re-enter the

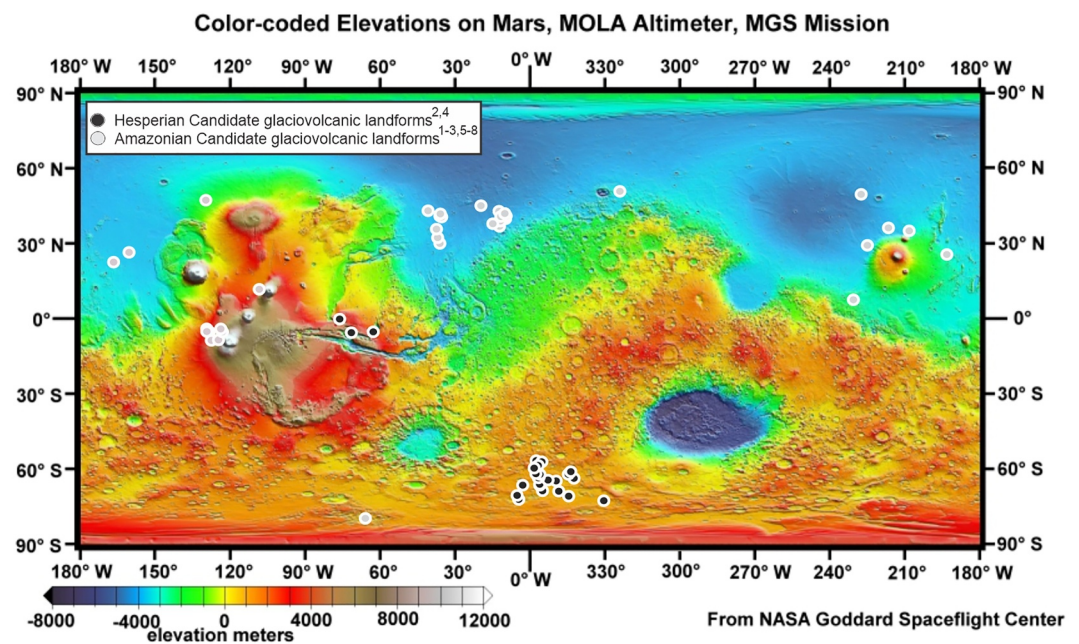


Figure 2. A Mars elevation map created using MOLA data from the Mars Global Surveyor mission showing the locations of candidate glaciovolcanic landforms. A list of citations used in this figure is provided in Table 1 with latitude and longitude of each candidate glaciovolcanic landform provided in Table S1.

Table 1
List of Citations Used in Figure 2

Reference number	Citation
1	C. Allen, (1979)
2	Chapman and Tanaka, (2001)
3	Chapman (2003)
4	Ghatan and Head, (2002)
5	Chapman (1994)
6	Martínez-Alonso et al. (2011)
7	Scanlon et al. (2014)
8	Kadish et al. (2008)
9	Hovius et al. (2008)

englacial lake forming well sorted, fine-grained hyalotuff beds with sedimentary features such as ripple laminations.

If the eruption continues, the volcanic edifice can breach the surface of the lake and the eruption style becomes effusive again, forming a coherent subaerial lava cap and volcanic crater. At this stage, a residual lake can exist around the growing volcanic edifice into which subaerial lava can flow, forming a lava delta as it quenches at the contact of the water and becomes hyaloclastite. Pillows formed as effusive subaerial flows enter into the water are usually brecciated as they are transported down the steep slopes of the glaciovolcano. This lava delta phase is usually termed the “passage zone” as it marks the transition into subaerial volcanism and the height of the ice cap at the time of the eruption. Meanwhile, subaerial eruptions largely generate thick stacks of pahoehoe or a’a lava flows with lava tubes, tumuli, or lava rises (Andrew & Gudmundsson, 2007).

2. Materials and Methods

2.1. The SAND-E Mission and 2019 Field Site

This study was conducted within the SAND-E: Semi-Autonomous Navigation for Detrital Environments NASA-funded Mars-analog mission whose main science objective was to characterize the physical and chemical evolution of basaltic sediment while transported from source-to-sink in cold and wet analog environments in Iceland. Iceland is a long-standing location for Mars-analog research due to its predominantly basaltic crust and the presence of volcanic and sedimentary environments similar to those that have occurred on Mars, such as glacial, fluvial, aeolian, and effusive and explosive volcanism (C. Allen et al., 1981; Carson et al., 2023; Cousins, 2015; Mangold et al., 2011; Thorpe et al., 2021). The SAND-E mission was undertaken to expand the knowledge of source-to-sink processes in basaltic glacio-fluvio-lacustrine sedimentary systems using analytical techniques available to the Curiosity and Perseverance rovers, supplemented with microscopic analysis (cf., Ewing et al., 2019 for more details on the SAND-E mission architecture).

The Þórisjökull glacio-fluvio-aeolian sedimentary system was selected as the 2019 field site of the SAND-E mission as it exists in a predominantly basaltic environment with primary igneous minerals akin to those that are abundant on Mars, such as basaltic glass, olivine, pyroxene, and feldspar (Eason et al., 2015; Jakobsson & Johnson, 2012; Sinton et al., 2005). As such, this field site provides an opportunity to investigate source-to-sink processes over short (15 km) distances for Mars-relevant basaltic materials and sedimentary systems and to do a thorough characterization of the source rocks given that they stem from four main volcanoes. This study focuses on characterizing the chemical and mineralogical characteristics of the source materials of the SAND-E 2019 mission, constraining the geological history and volcanology of an understudied area in SW Iceland, forming the basis of a future sediment analysis, in addition to providing insight into the potential geochemical and mineralogical signatures of glaciovolcanism on Mars.

Three days of the field trials were dedicated to sampling the source rock materials of Þórisjökull, Litla-Björnsfell, Stóra-Björnsfell, and Skjaldbreiður volcanoes out of mission simulation (Figure 3). The SAND-E 2019 campaign locality was situated in the Western Volcanic Zone (WVZ). The WVZ is one of four volcanic lineaments (WVZ, Mid-Iceland Belt, Eastern Volcanic Zone and Northern Volcanic Zone) which stretch across the Iceland volcanic plateau. These volcanic lineaments formed through the relative motion of spreading of the Mid-Atlantic Ridge coupled with increased melt generation from the Iceland mantle plume situated underneath (R. M. Allen et al., 1999, 2002; Thordarson & Larsen, 2007; Vink, 1984). Previous research on the Þórisjökull, Litla-Björnsfell, and Stóra-Björnsfell volcanoes within the WVZ is limited, but overall, ³He exposure ages show that they likely erupted toward the end of the Younger Dryas period of glaciation ~12.8–11.7 ka (Eason et al., 2015), whereas the Skjaldbreiður shield volcano erupted during the Holocene within 3,000 years after the Younger Dryas period of glaciation ended (between 6,000 and 9,000 ka) (Sinton et al., 2005). As such, periods of glaciation and deglaciation have played a significant role in shaping the geology of the area.

The Litla-Björnsfell and Stóra-Björnsfell volcanoes were sampled up stratigraphic section for each change in morphology observed between pillow basalt, hyaloclastite, hyalotuff, and capping flow (Figures 3 and 4). Due to

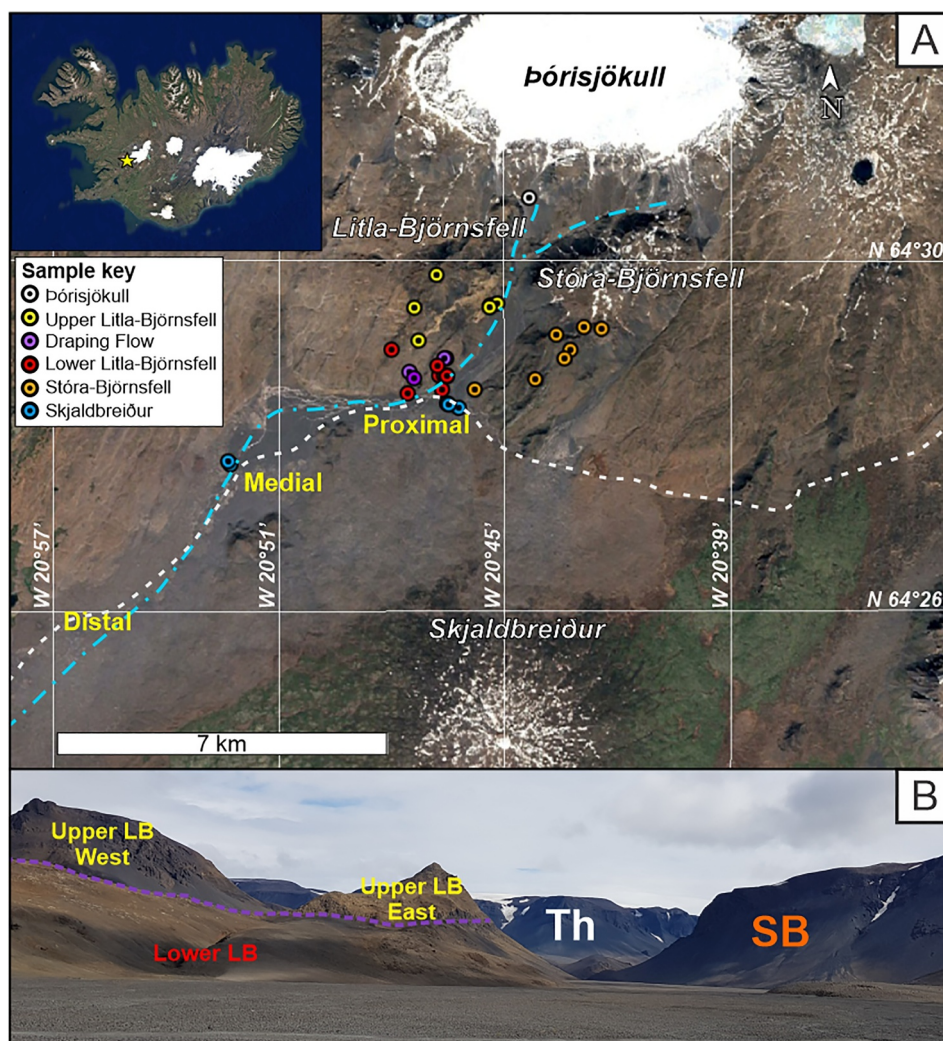


Figure 3. (a) A map of the SAND-E 2019 field locality with red dots showing the source rock sampling locations. The dashed white line shows the boundary of the Skjaldbreiður lava apron and the blue dot and dashed line show the sedimentary system under investigation by the SAND-E mission. Proximal, Medial, and Distal sites show the locations of the SAND-E 2019 sediment sampling campaign. The top left shows an insert of Iceland with the yellow star marking the site of the SAND-E 2019 field locality. (b) A field image of the main sampling area looking north from the Proximal site toward Þórisjökull. Glaciovolcanic units are labeled Th = Þórisjökull, LB = Litla-Björnsfell, Purple dashed line marks the location of the Draping Flow unit, SB = Stóra-Björnsfell.

poor weather conditions on the Þórisjökull sampling day, cobbles at the base of the glacial outwash fan were collected to represent the diversity of geological units situated within the volcano. GPS coordinates, images, and field sketches were acquired at each sampling site, and each sample was removed using a geological hammer. All volcanic samples were taken avoiding lichen or moss.

2.2. Geochemical Techniques

All samples were analyzed at NASA Johnson Space Center using the same pXRF and close-up imager that analyzed the sediments in the field and the laboratory, in addition to benchtop XRF, electron microprobe, and XRD, thus providing geochemical and mineralogical information on each glaciovolcanic facies with height in the volcanoes that relates to the sediment geochemical and mineralogical data acquired.

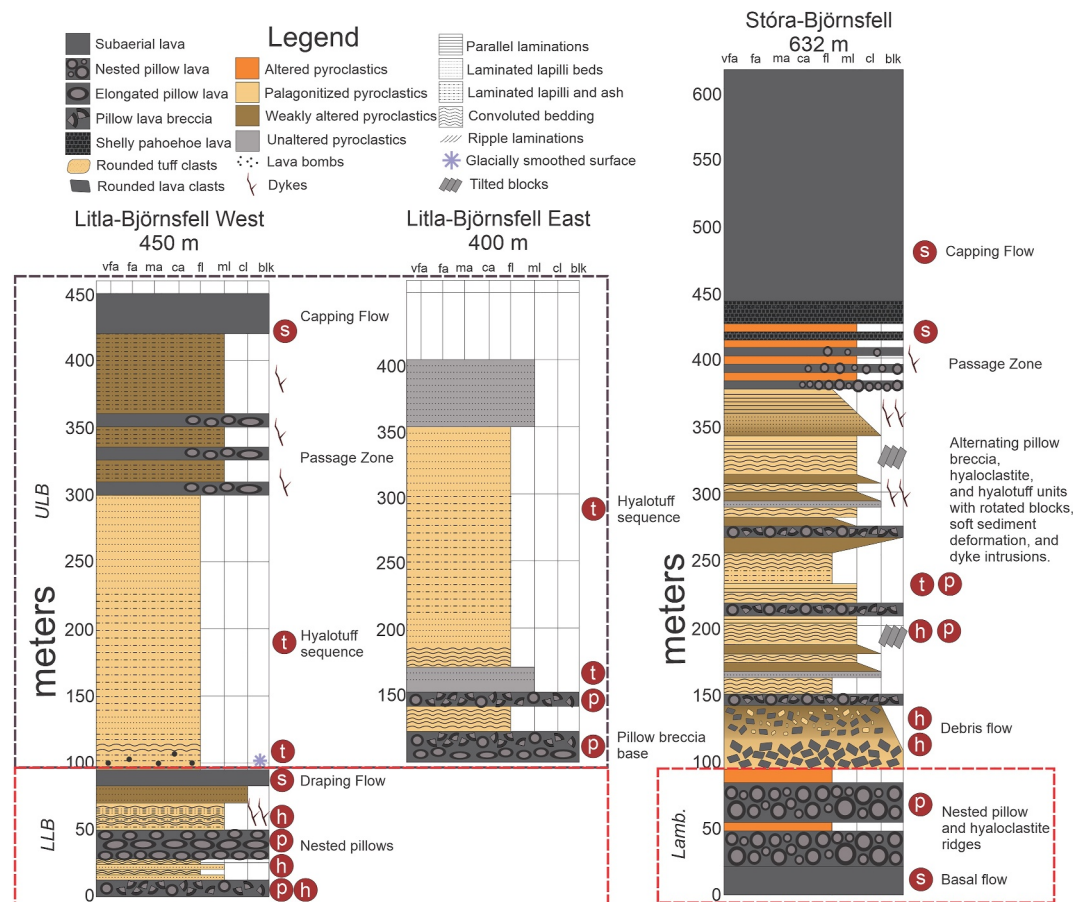


Figure 4. Representative vertical profiles of Litla-Bjornsfell and Stóra-Bjornsfell. Grain size determinations follow that of White and Houghton. (2006) and are; very fine ash (vfa 1/16–1/8 mm), fine ash (fa 1/8–1/4 mm), medium (ash 1/4–1/2 mm), coarse ash (ca 1/2–2 mm), fine lapilli (lp 2–4 mm), medium lapilli (l 4–16 mm), coarse lapilli (cl 16–64 mm), blocks/bombs (blk > 64 mm). Letters in red circles indicate sample locations and sample types where p = pillow, h = hyaloclastite, t = hyalotuff, and s = subaerial.

2.2.1. Portable X-Ray Fluorescence Spectroscopy and Benchtop X-Ray Fluorescence Spectroscopy

Bulk geochemical analyses of the sediments and source rocks of the SAND-E 2019 field site were collected with an Olympus Vanta M Series portable X-Ray Fluorescence (pXRF) analyzer to measure Si, Ti, Al, Fe, Mn, Mg, Ca, K, P, Ni, Cr, Co, Sr, Ba, Zn, Zr, and Cu. The pXRF model used during the field trials is a VCR (rhodium (Rh)) anode, silicon drift detector (SDD) system containing a 4 W X-ray tube. A thin proline film window was used to protect the detector during testing. The Vanta pXRF also contains a 5 megapixel camera that acquired images of the sample showing the analyzed area for each test. Corrections for temperature and air pressure were made with each analysis using a built-in thermostat and barometer and the energy scale resets with every test. pXRF was selected as the geochemical instrument for the SAND-E field trials as it utilizes XRF similar to the Alpha Particle X-ray Spectrometer (APXS) instruments on the Mars Exploration Rovers and the Mars Science Laboratory missions (Berger et al., 2020; Gellert et al., 2006). To make the results comparable to the APXS instrument on-board the MSL Curiosity rover, major elements were converted into oxides and normalized to 100 wt% (Gellert et al., 2006; Siebach et al., 2017).

Limitations of pXRF include relatively low limits of detection for light elements in comparison to a lab-based XRF instrument so not all elements can be quantified (e.g., Na and K), and that the results are influenced by the sample properties (i.e., grain size, moisture, heterogeneity). As such, sample preparation included sawing the volcanic rocks using a Bruker slab saw to reveal the fresh interiors. Then, to create a uniform grain size, the interiors were crushed with a hammer, ground using a quartz pestle and mortar, and milled with a McCrone Micronizing Mill using quartz beads and ethanol. Samples were dried and tightly packed into a sediment

container with a proline film. Each sample was tested for 3 min total to optimize data quality and analysis time as per the recommendation from the manufacturer. Prior to each day of analysis, a quartz standard was analyzed to check for contamination of grains on the proline film window.

Several samples collected during the 2019 field campaign were sent to Washington State University for benchtop XRF. Fused discs were made for these samples and were analyzed at the Peter Hooper GeoAnalytical Lab using a Thermo-ARL automated XRF (Daniel Steven Kelly, 2018; Johnson et al., 1999). Comparison of selected certified reference materials (AGV-2, BCR-2, and GSP-2) with their preferred values/GeoRem values were within expected uncertainties (see Data Set S3). Due to the better instrument accuracy of the benchtop XRF over the pXRF, we use benchtop XRF in most analyses. However, due to the ease of analysis using the pXRF and its capabilities for high precision, we use the pXRF to track elemental variations with height in the volcanoes.

2.3. Mineralogical and Petrographic Techniques

2.3.1. X-Ray Diffraction

Quantitative bulk mineralogy of the samples was acquired using a Rigaku Mini-Flex 6G X-Ray Diffractometer at the NASA Johnson Space with Co(K α) radiation. To prepare unaltered source rock samples for XRD analyses, we sawed off the exteriors to remove any lichen present on the surface in addition to sedimentary material trapped in the vesicles using a Bruker slab saw. Then, the interior was crushed using a hammer, followed by a quartz mortar and pestle to a fine sand grain size. Next, the samples were run through a McCrone Micronizing Mill with quartz beads and ethanol for 20 min to create a fine powder of uniform grain size (<10 μ m). Crushed and milled samples were then dried in an oven at 40°C overnight. Once dried, samples were homogeneously mixed with 20 wt% corundum added to the dried powders as an internal standard using a mortar and pestle. Samples were run in the Rigaku at a 40 kV voltage and 15 mA current with a scan range of 3°–70° θ and step size of 0.025° at 1.0°/min. XRD patterns were fitted using Profex-BGMN software (Doebelin & Kleeberg, 2015).

2.3.2. Electron Microprobe Analyses and Optical Microscope

Polished thin sections (30 μ m thick) were made by Wagner petrographic and carbon coated for analysis using the JEOL JXA-8530F and Cameca SX-100 electron microprobes at the NASA Johnson Space Center. Electron Backscatter Detection (EBSD) was used to identify different minerals (olivine, plagioclase feldspar, and pyroxene), glass, and palagonite grain coatings in the thin sections. When minerals, glass, and palagonite coatings were identified, we collected quantitative spot analyses (Data Set S2). Data were collected using a 15 kV accelerating voltage and 10 nA beam. The beam spot size was 5 μ m. See Data Set S2 for the list of standards used in the calibration.

An Olympus BX60 petrographic optical microscope was used to take plane-polarized and cross-polarized images of the thin sections to document the different textures in the volcanic samples.

2.4. Statistical Approach

In total, 27 samples were analyzed with benchtop XRF across the different volcanoes and morphological types. To determine whether geochemical variation was related to volcanic source or morphology, an agglomerative cluster analysis was performed on all samples except those relating to hyaloclastite or hyalotuff which had experienced alteration. For this analysis, we used Minitab 20.4 statistical software (2021). The Minitab algorithm defines each data point as a cluster and then combines the two closest clusters into a new one at each step (Schuenemeyer & Drew, 2011). In this study, we used the Euclidian measure of distance and the Complete method of determining linkage (see Text S1 and Tables S2–S4 in Supporting Information S1 for equations and the cluster analysis output). Variables used in the cluster analysis include all major, minor, and trace elements from the benchtop XRF data (SiO₂, TiO₂, Al₂O₃, FeO_T, MnO, MgO, CaO, Na₂O, K₂O, P₂O₅, Ni, Cr, Sr, Ba, Zr, Zn, V, Cu). Variables were standardized due to different magnitudes in abundance between SiO₂ and V so as not to bias the results toward the more abundant elements. The Minitab algorithm standardizes the variables by making all means equal 0 and their variance equal to 1.

The cluster output is graphically presented as a dendrogram with similarity level on the y-axis, where higher similarity levels represent stronger correlations between Clusters (see Text S1 in Supporting Information S1 for the equations used to calculate similarity and distance). As this cluster analysis is agglomerative and seeks to

combine all clusters, the similarity level can provide a useful guide on when clusters that are distinct are being combined, in which case there will be a marked step in similarity values between clustering steps. As a result, the similarity level is used to identify the number of Clusters in the data set according to the limits defined by the user. We defined the number of Clusters in this work according to where we saw an abrupt change in similarity values (difference in similarity is >5.00 where previously it was <1.00) between steps during the cluster analysis similar to the methods of Bedford et al. (2020).

3. Results

3.1. Geology

3.1.1. Stóra-Björnsfell

Stóra-Björnsfell has a characteristic table mountain morphology including steep sides comprising largely hyaloclastite and hyalotuff, and a cap containing subaerial lava and a crater (Figure 1c). Stóra-Björnsfell also contains a series of N-S trending linear ridges—the Lambahliðar—extending from its southern edge (Figure S1 in Supporting Information S1). The Lambahliðar consist of an eroded, basal, dyktytaxitic sheet flow exposed to the SW of Stóra-Björnsfell (Figure 4) and repeating sequences of pillow and hyaloclastite containing meter-thick vesicular pillow and pillow breccia interbedded with an orange lapilli tuff. Many of Iceland's volcanic eruptions occur as fissure eruptions and then localize to a central point. It is possible that the Lambahliðar represent the early stages of the Stóra-Björnsfell eruption.

The pillow and hyaloclastite units continue to the base of the main Stóra-Björnsfell volcano, after which there is ~ 20 m of a clast-supported conglomerate with cubic, poorly sorted, subangular clasts, 2–10 cm long within a yellow, ash and lapilli matrix that contains crude bedding ~ 30 cm thick (Figure 4). Clasts are blue/gray and contain vesicles with some imbrication present indicating a downslope flow direction to the south. 25 m of matrix-supported, moderately sorted conglomerate with subrounded clasts between 0.2 and 4.0 cm long occurs above the previous conglomerate (Figure 4 and Table 2). Clasts are either similar in appearance to the blue/gray clasts from the base of the mound unit but with fewer vesicles, or they are yellow with some laminations present. The blue/gray clasts have an average grain size along their intermediate axis of 1.4 cm, whereas the yellow clasts are on average 0.5 cm long and are more rounded than the blue/gray clasts. The matrix for this conglomerate consists of yellow-brown to dark-brown lapilli. This conglomerate also contains cm-scale bedding with some normal grading and imbrication of the larger clasts. This poorly sorted, heterolithic, normally graded deposit is interpreted to result from debris flows occurring in the later stages of volcanism as the volcanic edifice is erupting into a shallow englacial lake (Le Masurier, 2002; Skilling, 2002; Smellie, 2018). The cubic, sub-rounded blue clasts are likely rounded pillow breccia or clasts of subaerial capping flow with reworked clasts of hyalotuff from the top of the volcano edifice.

Above the conglomerates exists a 220 m thick repeating sequence of hyalotuffs for ~ 175 m with rare isolated pillows, pillow breccias and hyaloclastites whose occurrences are spatially variable (Figure 4 and Table 2). The hyalotuffs are well-sorted deposits with cm-scale convoluted bedding that vary in grain size from ash to coarse-lapilli and can contain rotated blocks and soft-sediment deformation features such as scours (Figure 4). Coarse lapilli (>10 mm diameter) have a high sphericity, and beds that are coarser-grained are darker in color. Lobes of pillow and pillow breccia interspersed throughout the hyalotuff range in size from ~ 30 cm to 2 m thick. Some smaller pillow lobes are present at the base of hyalotuff intervals with the pillows relatively intact though most show concentric jointing. These pillows are spherical, contain a thick quenched rim (2 cm thick) that can show a ropey texture, have some small vesicles (~ 0.5 cm diameter), and show large (~ 1 cm) plagioclase glomerocrysts concentrated toward the pillow core. Cross-sections of the more isolated pillow lava show several quench rims suggesting multiple growth stages. Larger pillow breccias appear to be at the top or middle of a hyalotuff interval and share a gradational contact with the hyalotuff on both sides. These pillows are much more fragmented, and the breccia is poorly sorted with clasts of a few cm to 10s of cm. Some large (~ 1 m long) elliptical pillows are intact with quenched rims and concentric jointing. These large elliptical pillows are surrounded by smaller brecciated pillow fragments in a coarse lapilli and ash tuff matrix. This unit is interpreted to have formed once the volcanism penetrated the top of the ice cap. Sorting occurs either in the ash cloud and the lapilli and ash re-enter the englacial lake or as a result of eruption-fed aqueous density currents transporting material down the slopes of the growing volcanic edifice (Jakobsson & Gudmundsson, 2008; White, 2000). Pillow breccias occur where lava flows re-

Table 2
Showing Outcrop and Close-Up Images of Distinct Morphological Units Within the SAND-E 2019 Field Site Along With Their Descriptions and Interpretations


Name	Outcrop image	Close-up image	Description	Interpretation
Block and Ash Flow			Massive, poorly sorted, bedded conglomerate with fractured angular to curved clasts 1–20 cm in scale that conform to the shape of the valley floor. Matrix is ash to fine lapilli in grain size with a tan to bright orange color. Clasts appear similar in color to the matrix with a few that exhibit vesicularity. Most clasts are fragmented and tuff-like in appearance	A block and ash flow confined to the valley floor, containing tuffaceous material like Upper LB East. Suggests the explosion or gravitational collapse of a growing lava dome
Debris Flow Deposit			Crudely bedded, matrix-supported conglomerate with heterolithic clasts and some imbrication indicative of downslope flow from the volcanic edifice. Beds appear to show some normal grading. Clasts are subangular to subrounded. Blue/gray clasts are vesicular and have an average grain size of 1.4 cm along the intermediate axis. Yellow clasts are on an average 0.5 cm long, some are laminated. Occasional small (~0.2 cm long), rounded, red clasts are also present. Matrix is dark brown with a mixture of lapilli and ash. Finger in picture is 3.5 cm long	A mixture of clasts from morphologies sourced higher up in the volcanic edifice (sorted tuff and vesicular basalt), imbrication, crude bedding, and matrix supported nature, suggests that this deposit formed because of a debris flow
Hyalotuff			Very fine to fine-grained ash and lapilli layers that show a medium to high degree of sorting. Normal grading is common as is bedding, parallel or cross-laminations, and soft-sediment deformation structures. Most lapilli grains are angular with a high degree of vesicularity. Some accidental clasts occur as rounded, dark, aphyllitic lapilli grains. Grains are cemented with palagonite ranging in color from yellow to dark brown. Black handle in picture is 20 cm long	Patagonite-cemented tuff formed from the eruption becoming explosive as lava erupted into a shallow englacial lake Sorting of lapilli and ash occurred in the surtsayan or plinian ash column and settled back into the lake forming thin beds with sedimentary features

Table 2
Continued

Name	Outcrop image	Close-up image	Description	Interpretation
Hyaloclastite			<p>Matrix supported conglomerate with discontinuous, wavy bedding that show variations in grain size. Some beds show normal sorting. Beds can also be fractured and tilted or contain resistant ridges</p> <p>Yellow to orange/brown palagonitic ash cements clasts. Larger clasts (~0.25 cm diameter) are subangular to subangular, dark gray, and contain small vesicles with a matte luster. Smaller clasts (~0.1 cm) are angular to subangular, black, with a vitreous luster</p>	<p>Palagonite-cemented lapilli-tuff formed from explosive and effusive fragmentation as lava erupted into an englacial lake</p>
Pillow Breccia			<p>Brecciated, angular to subangular, round, bulbous shapes (spherulic or elongate) often occurring in clast-supported beds. Some glassy rinds preserved. Occurs interbedded with bedded tuff deposits</p> <p>Same description as pillow basalt below. Can have a greater abundance of vesicles if erupted at shallower depths in the ice cap. This example has a greater abundance of feldspar and pyroxene phenocrysts</p>	<p>Subaqueous lava flow front deposit. Pillow basalts form from effusive subaqueous lava flow and brecciate due to quench fragmentation and transportation downslope</p>
Pillow/Kubbaberg			<p>Round, bulbous shapes (spherulic or elongate) can be in contact with each other (nested pillows) or surrounded by a finer grained hyaloclastite matrix. Glassy rinds can be preserved (up to 10 cm thick). Cube jointing (Kubbaberg) common</p> <p>More glassy toward exterior with greater vesicle abundance. Phenocrysts tend to accumulate toward center. Overall, aphanitic groundmass</p>	<p>Nested pillow basalts at base of volcano exhibiting cube-jointing due to quenching. Greater fragmentation around pillow lobes suggests fragmentation due to thermal and mechanical spalling. Low vesicularity indicates higher pressures</p>

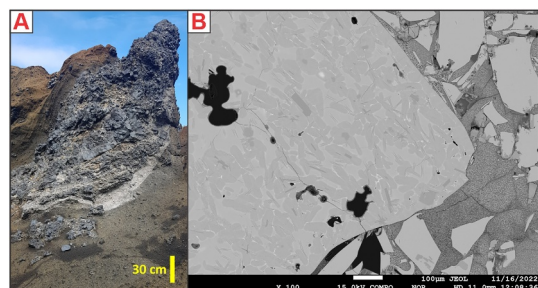


Figure 5. (a) Field image of a kubbaberg intrusion into hyaloclastite. Note the tilting of the beds and peperite margin. (b) Microprobe image of sample showing devitrification of a kubbaberg clast and the characteristics of the ashy matrix.

enter the lake and brecciate as they flow downslope, forming lava delta foresets or flow front breccias (Jakobsson & Gudmundsson, 2008; Le Masurier, 2002).

A unit dominated by thin beds of tuff interbedded with pillow lava and pillow breccia units sits above the hyalotuff unit and eventually grades into thin (<1 m thick), laterally consistent vesicular lava flows and multiple vertical dykes. Some dykes and flows share a red contact with the tuff. This interval is termed the passage zone as it likely reflects the transition from subaqueous to subaerial volcanism and extends for 130 m. The thin, vesicular lava flows at the top of this interval contain several small lava tubes (Figure S1 in Supporting Information S1) and express a shelly pahoehoe morphology with vertical jointing apparent throughout, though the weathering of the flow is extensive and pahoehoe surface textures are no longer apparent.

Above the passage zone interval is the capping flow that contains thick lava flows that have been extensively weathered into large blocks with an orange exterior (Figure 4 and Figure S1 in Supporting Information S1). Cross-sections of the blocks show a dyktaxitic texture with horizontal zones of vesicles. Feldspar phenocrysts are present as glomerocrysts. Some smaller mafic mineral phenocrysts are also present in the capping flow lava.

3.1.2. Litla-Björnsfell

Similar to Stóra-Björnsfell, Litla-Björnsfell consists of volcanic mounds that stratigraphically overlie NE-SW trending linear ridges. However, unlike Stóra-Björnsfell, Litla-Björnsfell's ridges and mounds are divided by a large subaerial capping flow. For this reason, Litla-Björnsfell (see Figure 4 for the representative vertical profile) has been divided into three main units: Lower Litla-Björnsfell, Draping Flow, and Upper Litla-Björnsfell (Figures 3 and 4). Litla-Björnsfell also has two NE-SW trending normal faults that have created a graben in Lower Litla-Björnsfell and the Upper Litla-Björnsfell volcanic mounds are divided into Upper Litla-Björnsfell East and West. Within this graben lies a block and ash flow deposit that extends from Upper Litla-Björnsfell East, suggesting that there was a collapse of this volcanic edifice into the graben during or shortly after its formation (Table 2).

3.1.2.1. Lower Litla-Björnsfell

Lower Litla-Björnsfell contains an 82 m thick series of pillow lobes and pillow breccias at its base that occur in sequence with hyaloclastite tuff deposits (Figure 4 and Table 2). The pillow breccias are ~5 m wide and several meters thick and appear to scour into the hyaloclastite, suggesting that they followed the deposition of the hyaloclastite units. Pillow breccias are mostly clast-supported in the center of the deposit and matrix-supported toward the edge of the deposit. Pillow clasts commonly show a quenched rim, small vesicles (<1 mm), and an aphanitic texture (Figure 5a). Small (<1 cm) phenocrysts of plagioclase feldspar and olivine are rare but present in some samples. Higher in elevation, large (~1 m thick), elongate, nested pillow lobes are present. Here, cube-jointing within the pillow lobes and quenched rims on the exterior of the pillow lobes are common.

The hyaloclastite deposits are thinly bedded (~5 cm thick) with convoluted bedding common in finer grained units. Clast size varies between beds, showing poorly developed normal grading of clasts between 0.1 and 2 cm diameter. Clasts are aphanitic, rounded, and moderate to well-sorted containing few vesicles. The matrix of the hyaloclastite largely consists of ash to lapilli-sized sideromelane grains coated in an orange palagonite.

Higher in the volcanic edifice, intrusions of cube-jointed basalt occur into the hyaloclastite, some with white reaction margins that contain fragmented parts of the basalt intrusion, with fragments decreasing in size with distance from the intrusion into the tuff (Figure 5). These are interpreted to be peperite deposits with EBSD images revealing that the white matrix is unaltered ash, which indicates that the basalt intrusions formed while the tuff was still wet and relatively un lithified, causing quenching of the magma and the fluidization of the hyaloclastite upon emplacement (Skilling et al., 2002; van Otterloo et al., 2015). Overlying hyaloclastite deposits have steep bedding orientations around the basalt intrusions, suggesting that they were tilted during the emplacement of the intrusion.

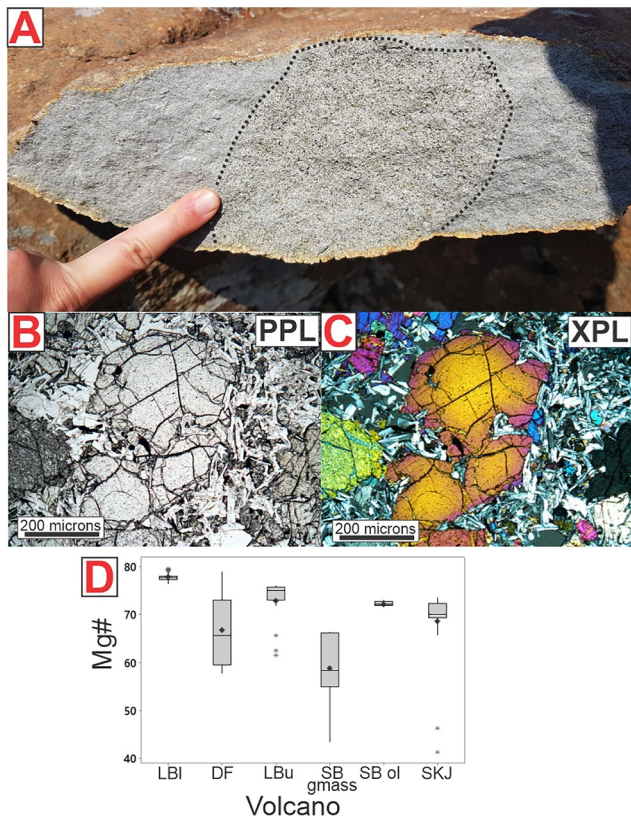


Figure 6. (a) Field image of the Draping Flow after a sample was acquired with a geological hammer and the fresh interior was exposed. The dashed circle shows the boundary of the coarsely crystalline picrite nodule. (b) A plane-polarized and (c) cross-polarized image of an olivine mineral within the picrite nodule showing zoned rims and disequilibrium/resorption textures. (d) Boxplots of Mg number of olivine grains from lower Litla Björnsfell (LBI), the Draping Flow (DF), Upper Litla Björnsfell (LBU), Stóra-Björnsfell groundmass (SB gmass) and phenocrysts (SB ol), and Skjaldbreiður (SKJ). Data were acquired using the microprobe. The dark circle represents mean abundances, and stars show outlying values.

3.1.2.2. The Draping Flow

Capping the Lower Litla-Björnsfell plateau is a weathered subaerial lava flow that varies in thickness between 10 cm and 3 m in places (Figure 4), which we have termed the Draping Flow. This lava flow's surface is an orange/red color and has been weathered into blocks exposing vesicle zonation in places. The Draping Flow has been smoothed with pahoehoe structures rarely preserved. The flow is crystalline with a light gray groundmass containing white laths of fine feldspar minerals and large phenocrysts of green olivine and pyroxene. In places, the Lower Litla-Björnsfell capping flow has nodules of coarsely crystalline olivine-rich picrite that have a sharp boundary with the surrounding lava (Figure 6a). The Lower Litla-Björnsfell capping flow scours into the westernmost hyaloclastite ridge and appears to bank against the northern flank of the Þórisjökull volcano suggesting that it formed later in the geological record.

3.1.2.3. Upper Litla-Björnsfell

Upper Litla-Björnsfell consists of two mounds that stratigraphically overlie the Lower Litla-Björnsfell capping flow and are separated by a valley. The westernmost mound largely consists of a dark brown hyalotuff that extends from approximately 100–300 m. The hyalotuff is thinly bedded (1–4 cm thick) with beds containing moderate to well-sorted lapilli that vary in grain size between the beds. Clasts of vesicular tachylite and some lava bombs are present in the tuff beds along with slump features and convoluted bedding. From 300 m to the summit at 450 m Upper Litla-Björnsfell has hyalotuff that is interbedded with cube-jointed lava. The cube-jointed lava occurs in meter-scale beds with the occasional small lava tube present at the top indicative of a passage zone and thin capping unit (Figure 4).

The easternmost mound stratigraphically overlies the Draping Flow and largely contains yellow hyalotuff that is mostly well-sorted, shows normal grading between the beds of sideromelane clasts in a palagonitized ash and lapilli matrix, and has soft sediment deformation features such as convoluted bedding and scours (Figure 4). Some hyalotuff beds have not been as extensively altered and are black in color with the lapilli grains containing a vitreous luster and only minimal yellow palagonite matrix (Figure 4).

Lapilli grains in these tuff deposits are very vesicular with some displaying a cauliflower structure (Figure 7c) and are sorted into mm-scale laminations that occasionally display ripple lamination. About midway up the eastern Upper Litla-Björnsfell mound (~150 m) is a dark-toned unit that extends laterally across the mound, decreasing in elevation toward the south until it reaches the contact of Upper Litla-Björnsfell with Lower Litla-Björnsfell. Due to the unstable nature of the eastern Upper Litla-Björnsfell mound, we were unable to investigate this in situ, however, boulders at the base of debris fans extending from this unit contained subangular vesicular basalt clasts present as pillow breccia in one particularly large boulder, and large vesicular pillows (~0.3 m diameter) with concentric jointing in another boulder.

A yellow branch of tuff extends from Upper Litla-Björnsfell into the floor of the graben, overlying the weathered capping flow and beds of diamictite present amongst the capping unit and seemingly following the contours of the valley. This yellow branch is a very pale-yellow conglomerate of poorly sorted, angular and distorted clasts of reworked tuff, some containing laminations (Table 2). The conglomerate is a matrix supported with yellow ash. This unit is welded with some clasts showing a red hue on some surfaces, indicating that this deposit formed at a high temperature. This deposit is interpreted as a block and ash flow deposit that formed from the collapse of the Upper Litla-Björnsfell edifice in the latter stages of its formation.

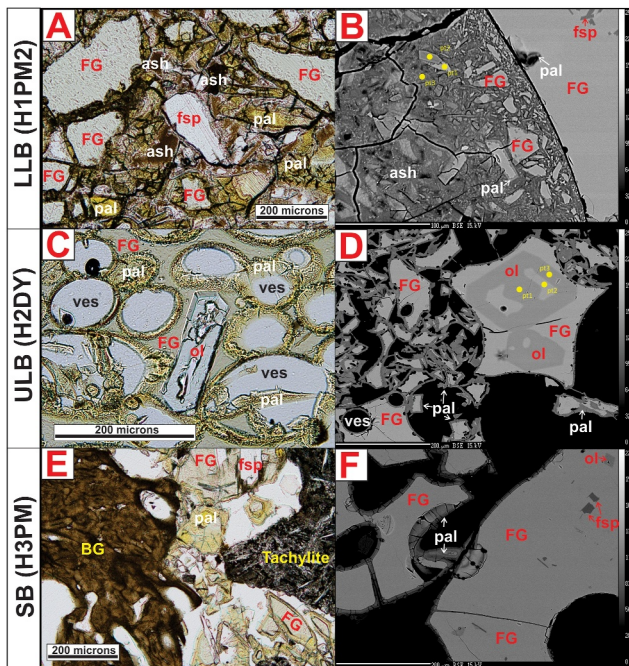


Figure 7. Plane polarized light optical microscope images (a, c, and e) and electron backscatter images (b, d, and f) of hyaloclastite tuff and hyalotuff samples taken from Lower Litla-Björnsfell (LLB), Upper Litla-Björnsfell (ULB), and Stóra-Björnsfell (SB). FG = sideromelane, pal = palagonite, ol = olivine, ves = vesicle, fsp = feldspar, BG = brown glass.

3.1.3. Skjaldbreiður

Skjaldbreiður is a large shield volcano present to the south of the field site (Figure 1d) with an estimated volume of at least 25 km³ (Andrew & Gudmundsson, 2007). Skjaldbreiður has two main units; the lower lava apron that extends to the Proximal site and consists of thick flows (up to 1 m thick), large tumuli and lava rises (several meters tall), and pahoehoe structures, and the upper lava apron that consists of thin lava flows (<0.5 m thick) with thin, abundant pahoehoe features (Andrew & Gudmundsson, 2007). We sampled the lowermost lower lava apron closest to the Proximal and Medial field sites. These samples were vesicular with a diktytaxitic texture that included glomerocrysts of feldspar, olivine, and pyroxene.

3.2. Geochemistry and Mineralogy

3.2.1. Subaerial and Subglacial Lava

For this study, samples have been categorized as altered (hyaloclastite and hyalotuff), unaltered (freshly exposed interiors of subaerial flow and subglacial pillow samples), and glass (pillow rinds, scoria). The geochemistry of Litla- and Stóra-Björnsfell unaltered subglacial lava (pillow and kubbaberg) and subaerial lava morphologies shows some significant changes according to the stratigraphic unit. For Stóra-Björnsfell (blue markers in Figure 8), pXRF analyses from the Lambhliðar and main mound of non-tuff samples are geochemically and mineralogically similar to one another and show a trend toward slightly higher Sr and Zr abundances and lower Mg# with increasing height, indicative of continued fractional crystallization during the eruption. Consequently, the XRD data of Stóra-Björnsfell show a decrease in olivine relative to feldspar with elevation supporting fractional crystallization processes.

Litla-Björnsfell shows a clear divide in geochemical compositions between Lower Litla-Björnsfell, Draping Flow picrite, and Upper Litla-Björnsfell. Lower Litla-Björnsfell and Draping Flow samples that are not picritic have lower abundances of incompatible elements (e.g., Sr and Zr) than Upper Litla-Björnsfell. Picritic draping flow samples have high magnesium numbers (>65%) and very low incompatible elements. The high Mg# of the Draping Flow picrite correlates with high olivine abundances (46.0 wt% olivine, Figure 8e). When considering the crystalline component, Lower Litla-Björnsfell and Upper Litla-Björnsfell are not substantially mineralogically different with regard to relative abundances of pyroxene, feldspar, and olivine; however, similar to Stóra-Björnsfell, Upper Litla-Björnsfell displays a slight decrease in Mg# with height correlating with a loss of olivine. Mineral chemical compositions vary noticeably between Lower Litla-Björnsfell and Upper Litla-Björnsfell, with Upper Litla-Björnsfell pyroxenes containing higher FeO abundances and the plagioclase feldspar containing less CaO, and more Na₂O and K₂O. These more evolved mineral chemical compositions and the substantially higher SiO₂ bulk abundance of Upper Litla-Björnsfell rocks relative to Lower Litla-Björnsfell rocks is indicative of a much greater degree of fractional crystallization between these two volcanic units compared to what was seen to have occurred with height in Stóra-Björnsfell.

A cluster analysis supports that the main influence on the geochemical composition of subglacial and subaerial lava was the volcanic source and fractional crystallization processes (Figure 9a and Table 3), grouping Stóra-Björnsfell and Litla-Björnsfell with the other volcanoes in the area (Þórisjökull and Skjaldbreiður). Five clusters were identified; Cluster 1 had the most CaO (13.35 ± 0.01 wt%) and contained samples from Lower Litla-Björnsfell and the black pebble of Þórisjökull; Cluster 2 had the highest MgO (23.12 ± 0.45 wt%), Ni (820 ± 18 ppm), and Cr (2,039 ± 91 ppm) and represents the picritic samples of the Draping Flow; Cluster 3 had the most TiO₂ (1.41 ± 0.17 wt%), P₂O₅ (0.13 ± 0.01 wt%), Sr (179 ± 15 ppm), and V (284 ± 22 ppm), and is derived of samples from Stóra-Björnsfell and Skjaldbreiður; Cluster 4 contains a pale pebble from Þórisjökull and has the highest Al₂O₃ (17.73 wt%), and finally Cluster 5 has the most SiO₂ (50.22 ± 0.79 wt%), Na₂O (2.14 ± 0.09 wt%), K₂O (0.40 ± 0.07 wt%); Ba (108 ± 15 ppm), and Zr (78 ± 7 ppm), and contains samples from Upper Litla-Björnsfell. The cluster analysis shows that Clusters 3 and 5 (Stóra-Björnsfell, Skjaldbreiður, and

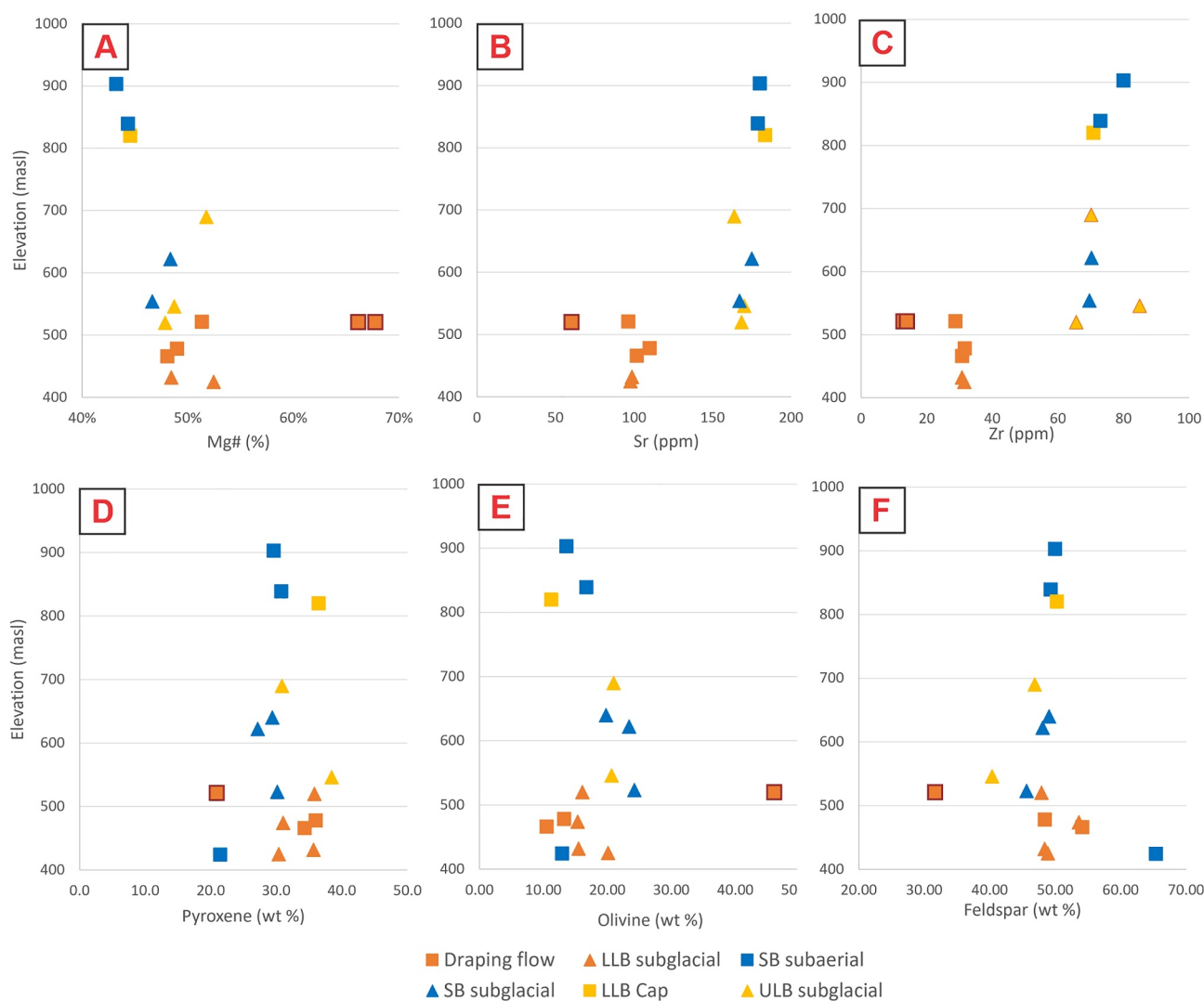


Figure 8. Geochemical and mineralogical variations with elevation for Stora-Bjornsfell (SB subglacial and SB subaerial), Lower Litla Bjornsfell (LLB subglacial), Upper Litla Bjornsfell (ULB), and the Draping Flow. Geochemical data were acquired with the pXRF while mineralogical data were acquired with XRD. Draping Flow squares with brown borders represent picrite analyses.

Upper Litla-Björnfell) are overall distinguished from Clusters 1, 2, and 4 by higher TiO_2 , Na_2O , K_2O , P_2O_5 , Sr, Ba, Zr, and Zn. Clusters 1, 2, and 4 have on average higher abundances of MgO and Ni compared to Clusters 3 and 5. Clusters 1 and 4 are largely distinguished by their SiO_2 and CaO abundances and substantially lower MgO, Ni, and Cr.

XRD results show that the high CaO abundance of Cluster 1 relative to the other clusters can be attributed to a high abundance of pyroxene (33.6 wt%) (Figure 10). The XRD patterns were fit by both diopside and augite crystal structures and microprobe data support the existence of these pyroxenes with a mean chemistry of $\text{Wo}_{[45\pm 1]}\text{En}_{[44\pm 4]}\text{Fs}_{[11\pm 3]}$ showing that augite present in these samples are high in calcium. Feldspar chemistries acquired from Cluster 1 samples (H1P1 and H1W1) also have the highest CaO abundances of all samples ($\text{An}81 \pm 3$).

Cluster 2's high MgO, Ni, and Cr likely relate to samples in this cluster having the most olivine (46.0 wt%). Cluster 2 pyroxene chemistry derived from microprobe data is indicative of diopside and augite, similar to Cluster 1 pyroxenes, but with a higher magnesium abundance (average of $\text{Wo}_{[46\pm 1]}\text{En}_{[49\pm 1]}\text{Fs}_{[6\pm 1]}$). The chemical composition of the interstitial feldspars in Cluster 2 samples are variable with an average $\text{An}75 \pm 25$.

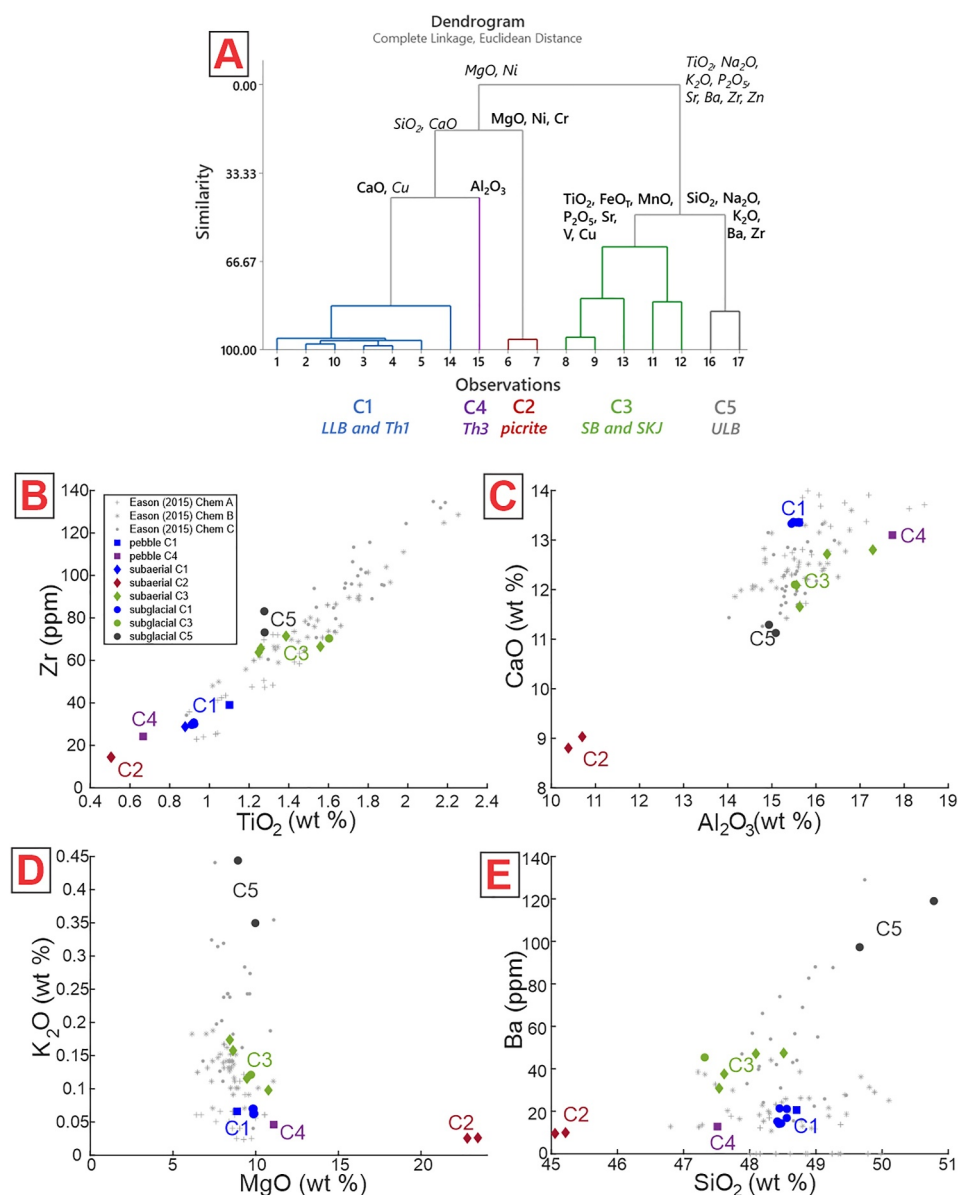


Figure 9. Results of the hierarchical cluster modeling of benchtop XRF data for non-tuff subglacial and subaerial samples. (a) Cluster dendrogram with calculated similarity levels on the y-axis. LLB = Lower Litla-Björnsfell, Th1 = Þórisjökull pebble 1, Th3 = Þórisjökull pebble 3, SB = Stóra-Björnsfell, SKJ = Skjaldbreiður, ULB = Upper Litla-Björnsfell. Elements in bold illustrate that this cluster has the highest abundance of the emboldened element relative to the other clusters. Italicized elements show elevated abundances relative to most clusters (but not the highest). (b–d) Element bi-plots comparing cluster results to XRF geochemical groups of surrounding glaciovolcanoes from Eason et al. (2015).

Cluster 3 is mineralogically similar to Cluster 1 but with slightly more olivine (17.1 wt% in Cluster 3, 12.1 wt% in Cluster 1) and less pyroxene, indicating that the geochemical differences in TiO₂, Na₂O, K₂O, P₂O₅, Sr, Ba, Zr, and Zn likely relate to a higher abundance of incompatible elements and more albitic feldspar phenocrysts (An₇₆ ± 7). Microprobe data show that pyroxene chemistries exhibit a large range that are all situated within the augite chemical field (Figure S2 in Supporting Information S1), while XRD pattern fitting suggests the presence of diopside in some samples. Overall, the chemistry of the pyroxenes is more calcium-poor and iron-rich (average Wo_[37±5]En_[44±5]Fs_[19±5]) compared to previous clusters.

Cluster 4 has the most plagioclase feldspar (60.0 wt%) in the XRD results, explaining the high Al₂O₃ abundance, alongside 14.9 wt% olivine and 25.0 wt% pyroxene. Diopside provided the best fit for pyroxene in the XRD

Table 3
Cluster Results Showing Average Compositions of Each Cluster, and Their Standard Deviations

Cluster	SiO ₂	±	TiO ₂	±	Al ₂ O ₃	±	FeO _T	±	MnO	±	MgO	±	CaO	±	Na ₂ O	±	K ₂ O	±	P ₂ O ₅	±	No.
1	48.52	0.10	0.95	0.07	15.56	0.07	9.79	0.16	0.17	0.00	9.73	0.38	13.35	0.01	1.81	0.04	0.07	0.00	0.06	0.01	7
2	45.14	0.11	0.50	0.00	10.54	0.22	10.49	0.05	0.18	0.00	23.12	0.45	8.92	0.16	1.06	0.01	0.03	0.00	0.03	0.00	2
3	47.81	0.48	1.41	0.17	16.05	0.75	10.63	0.70	0.18	0.01	9.40	0.94	12.27	0.48	1.97	0.09	0.13	0.03	0.13	0.01	5
4	47.51	*	0.67	*	17.73	*	8.10	*	0.14	*	11.09	*	13.10	*	1.57	*	0.05	*	0.05	*	1
5	50.22	0.79	1.28	0.00	15.01	0.11	10.00	0.19	0.17	0.00	9.45	0.74	11.21	0.12	2.14	0.09	0.40	0.07	0.12	0.00	2
R-sq	94.6		92.0		95.8		74.6		73.5		98.4		97.2		96.9		95.9		98.3		
p-value	0.000		0.000		0.000		0.001		0.002		0.000		0.000		0.000		0.000		0.000		

Cluster	Ni	±	Cr	±	Sr	±	Ba	±	Zr	±	Zn	±	V	±	Cu	±	No.
1	168	18	427	64	108	8	18	3	31	3	68	2	269	7	130	8	7
2	820	18	2039	91	63	0	10	0	14	0	69	1	174	0	69	1	2
3	164	40	327	62	179	15	42	7	68	3	83	7	284	22	136	7	5
4	238	*	231	*	126	*	13	*	24	*	54	*	199	*	75	*	1
5	177	26	457	56	169	1	108	15	78	7	83	0	267	5	119	1	2
R-sq	98.8		99.0		95.2		96.7		98.1		84.9		90.9		94.1		
p-value	0.000		0.000		0.000		0.000		0.000		0.000		0.000		0.000		

Note. Different colors indicate which cluster has the highest abundances (red) and lowest abundances (blue) of each composition. R² values and p-values show the results of the two-way Analysis of Variance that tests whether these clusters are statistically distinct from one another. In the ANOVA test, p-values < 0.05 are statistically significant.

pattern for this rock. We do not have microprobe data for this sample, but the similar bulk CaO concentration and strong overall similarity to Cluster 1 in the cluster analysis suggests that the pyroxene compositions are likely to have a comparably high-calcium composition.

Cluster 5 has the highest abundance of X-ray amorphous material (22.8 wt%), with similar incompatible element abundances to Cluster 3. Microprobe data have shown that the high SiO₂, Na₂O, K₂O, and Ba abundances of Upper Litla-Björnsfell samples from this cluster can be attributed to the low anorthite content of the feldspar

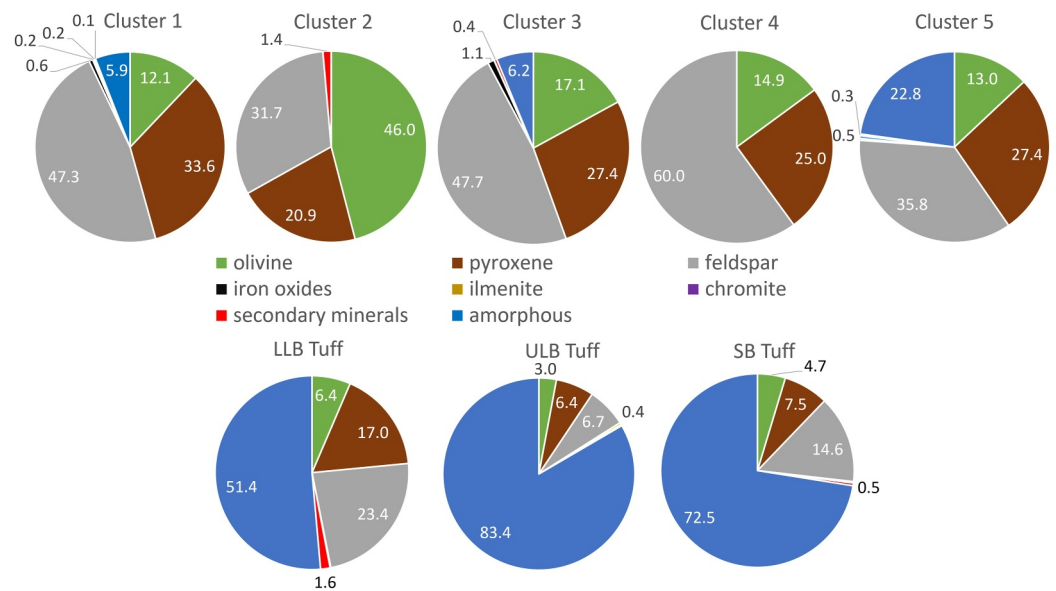


Figure 10. XRD results showing average bulk mineralogy of each cluster classification and average mineralogy of the different hyaloclastite (tuff) samples from different volcanoes. LLB = Lower Litla-Björnsfell, ULB = Upper Litla-Björnsfell, SB = Stóra-Björnsfell.

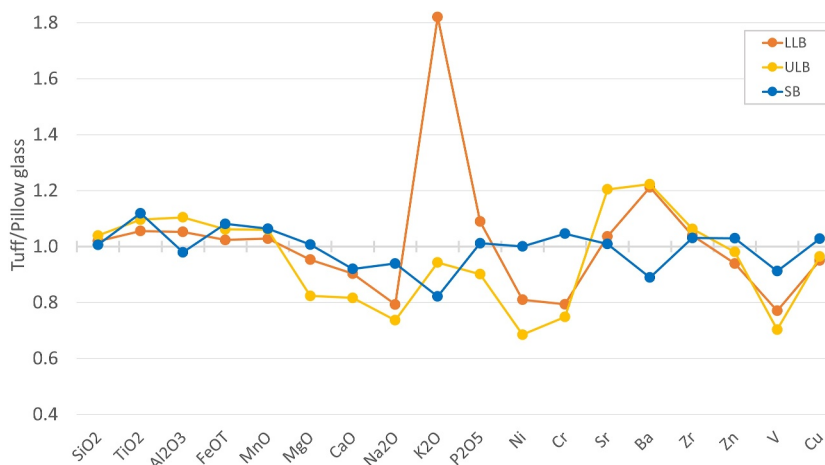


Figure 11. Benchtop XRF data showing the ratio of hyaloclastite and hyalotuff (tuff) samples to glassy pillow rinds from the same volcano. Arrows indicate significant element enrichment and depletion associated with palagonitization of the tuffaceous samples.

phases ($An_{69 \pm 5}$). K_2O is also high in Cluster 5's volcanic glass (see Upper Litla-Björnsfell glass compositions in Figure 12). Pyroxene compositions and XRD pattern fitting results are indicative of a both diopside and augite, but with a lower MgO and higher FeO abundance ($Wo_{[45 \pm 1]}En_{[35 \pm 3]}Fs_{[19 \pm 4]}$) than the other cluster groups.

All subglacial and subaerial samples (excluding hyaloclastite and hyalotuff) plot within the basalt igneous field of a total alkali versus silica plot and lie along a linear trend from the draping flow picrite composition (Cluster 2) to the Upper Litla-Björnsfell subglacial compositions (Cluster 5) (Figure S3 in Supporting Information S1), indicative of fractional crystallization or crystal accumulation driving the chemical differences of these samples from the majority. Most of the samples along this trend are clustered at ~ 48 wt% SiO_2 , suggesting that fractional crystallization is unlikely to be the main cause of geochemical variation between Lower Litla-Björnsfell (Cluster 1), Stóra-Björnsfell and Skjaldbreiður (Cluster 3), and Þórisjökull (Clusters 1 and 4).

3.2.2. Hyaloclastite and Hyalotuff

Overall, the hyaloclastite and hyalotuff morphologies (collectively referred to here as tuffaceous for simplicity) of the subglacial volcanoes are the most distinctive in geochemistry (Figure 11) and mineralogy (Figure 10). Benchtop XRF data of tuffaceous samples normalized against their unaltered subaerial and subglacial lava counterparts show that hyaloclastite and hyalotuff samples consistently show a 10% increase in TiO_2 , >5% increase in FeO_T , and >5% increase in MnO, and a notable decrease in CaO (10%–20%), Na_2O (10%–30%) and V (10%–30%) (Figure 11). Other elements are more variable; tuffaceous samples from Litla-Björnsfell (Upper and Lower) show an increase in Al_2O_3 (10%), and Ba (20%), and a decrease in Ni (>20%), and Cr (>20%) compared to the unaltered subglacial lava morphologies. Lower Litla-Björnsfell tuffaceous samples have a high abundance of K_2O , 1.8x that of its subglacial lava morphologies, while Upper Litla-Björnsfell tuffaceous samples are $\sim 20\%$ depleted in MgO and $\sim 10\%$ depleted in K_2O . Finally, Stóra-Björnsfell tuffaceous samples are most depleted in K_2O ($\sim 20\%$) and Ba ($\sim 10\%$) compared to their subglacial and subaerial lava morphologies. These geochemical variations in the benchtop XRF data between tuffaceous samples and their non-tuffaceous morphologies likely show different degrees of palagonitization of the volcanic glass, pillow breccia, and phenocrysts that derive the clasts in the samples and fluid flow between K_2O -rich Upper Litla-Björnsfell and K_2O -poor Lower Litla-Björnsfell.

Microprobe data comparing unaltered glass phases with palagonite cement in the tuffaceous samples support an increase in TiO_2 abundances and a decrease in CaO and Na_2O abundances with palagonitization of the glass (Figure 12). The increase in TiO_2 is less defined with some compositions showing less TiO_2 than the unaltered glass phase, and the increase in abundance for FeO_T and MnO is not apparent. However, a comparison of the palagonite compositions with compositions of other phases in the sample suggests that some palagonite alteration targets likely came from the alteration of mineral endmembers as well as the alteration of volcanic glass

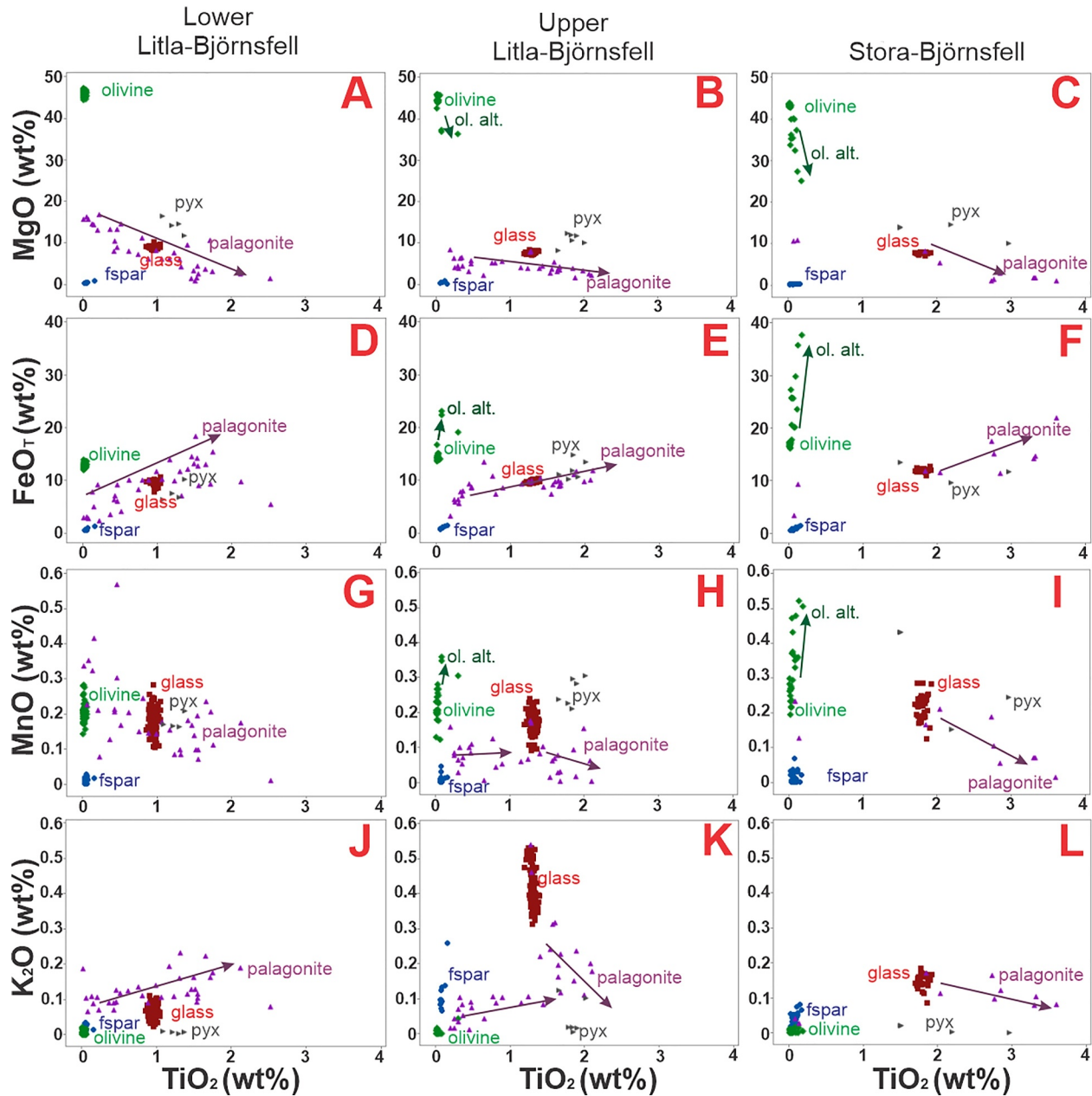


Figure 12. MgO, FeO_T, MnO, and K₂O versus TiO₂ scatter plots showing microprobe data for sideromelane (glass), palagonite, feldspar (fspar), pyroxene (pyx), olivine, and altered olivine (ol. alt.) grains. Arrows indicate apparent trends relating to alteration and palagonitization where present. Data are from tuffaceous subglacial samples taken from Lower Litla-Björnsfell, Upper Litla-Björnsfell, and Stóra-Björnsfell.

(Figure 12). This is particularly true for tachylitic samples (H1P1 from Lower Litla-Björnsfell and H2DB from Upper Litla-Björnsfell) whose groundmass is microcrystalline and not sideromelane. As XRF data is more representative of the bulk chemistry, the change in FeO_T and MnO abundances between tuffaceous samples and non-tuffaceous samples in the benchtop XRF data may be attributed to alteration of minerals and glass instead of only volcanic glass as the samples with the greatest enrichment of FeO_T and MnO (Upper Litla-Björnsfell and Stóra-Björnsfell) also show scatter toward higher FeO_T and MnO abundances in the olivine phenocryst phases (Figure 12). Microprobe data also support variable chemical differences in Al₂O₃, MgO, and K₂O for the palagonite in tuffaceous samples that may relate to different fluid compositions or aqueous alteration histories for each volcanic mound.

XRD data of the tuffaceous samples show that all of them are dominated by an X-ray amorphous material that derives >50 wt% of the bulk sample (Figure 10). Thin section images show that most of the X-ray amorphous material is unaltered volcanic glass according to their colorless isotropic appearance, occasionally containing phenocrysts with quench textures such as hollow olivine and skeletal feldspar phenocrysts (Figure 7). All volcanic glass grains are surrounded by an altered, fine-grained, yellow, isotropic cement (gel palagonite) or fine grained, isotropic, brown altered ash (Figure 7). Sideromelane dominates the volcanic glass grains present in all samples, especially Upper Litla-Björnsfell (samples H2DY and H2BC) that only shows grain diversity with regard to vesicularity and skeletal phenocryst grains. Tuffaceous samples from Lower Litla-Björnsfell (H1PM2) and Stóra-Björnsfell (H3PM1) show grain diversity with larger clasts of tachylite present, likely previous pillow or kubbaberg basalt incorporated into the tuff during formation (Figure 7). Stóra-Björnsfell tuffaceous samples also have some dark brown, vesicular glass grains present and Lower Litla-Björnsfell tuffaceous samples have individual phenocryst grains suspended within the altered ash matrix. Samples H2BC and H2DY of Upper Litla-Björnsfell and H3PM1 from Stóra-Björnsfell have yellow gel palagonite alteration rims around most grains, indicating that the cement formed from the interaction of the volcanic glass grains with water in the pore spaces. The yellow gel palagonite is also present in samples from Lower Litla-Björnsfell, but most palagonite cement in these samples has an orange/brown appearance indicative of a greater maturity in palagonite than from other tuffaceous samples in the area (Figure 7).

4. Discussion

The most notable difference between volcanoes that have erupted under an ice cap and those that have not erupted in the presence of an ice cap is the steep-sided, often flat-topped tuya or tinder landform and the formation of the pillow lava, hyalotuff, and hyaloclastite that give subglacial volcanoes their unique morphologies (Figure 1) (Jakobsson & Gudmundsson, 2008; Pedersen et al., 2020; Sigvaldason, 1968). Based on the vertical profiles of the glaciovolcanic landforms in this study (Figure 4), the tuffaceous units derive over half of Litla-Björnsfell and approximately half of Stóra-Björnsfell, whereas they are not present in the subaerial Skjaldbreiður shield volcano.

Pillow lava, hyaloclastite and hyalotuff morphologies are also present in other volcanic landforms that have erupted into a water column, such as a groundwater reservoir, an ocean, or a lake (Németh & Kósik, 2020). The main distinguishing factor between glaciovolcanism and other hydrovolcanic deposits largely lies in the landform itself as the ice confinement of the englacial lake and changes in lake level creates steeper, taller deposits that may have “benches” such as the Hlöðufell volcano (Jakobsson & Gudmundsson, 2008; Németh & Kósik, 2020; Pedersen & Grosse, 2014; Skilling, 2009). Both glaciovolcanic and submarine volcanic landforms can have a progression of morphologies from pillow lava and hyaloclastite at the base, to hyalotuff and eventually an effusive, subaerial cap once the volcanic edifice has breached the top of the water column (Honnorez & Kirst, 1975; Jakobsson & Gudmundsson, 2008; White et al., 2015). However, other phreatomagmatic landforms, such as maar and tuff cones, do not commonly have pillow lava and are dominated by hyalotuff deposits with a higher abundance of accidental fragments (Németh & Kósik, 2020; Ryan et al., 2024).

Previous studies have found a cyclical variation in geochemistry and mineralogy of the crystalline lava units that erupt during a period of glaciation, toward the end of a period of glaciation, and in a period of no glaciation (Andrew & Gudmundsson, 2007; Eason et al., 2015; Maclennan et al., 2002). It is possible that these cyclical variations may be unique to areas that have experienced multiple episodes of volcanism throughout glacial-interglacial periods as this can drive large changes in lithostatic pressure on the crust from the presence or absence of an overlying ice cap, which geophysical, geochemical, and tephrochronology studies suggest may impact rates of volcanism and shallow magma chamber formation (Andrew & Gudmundsson, 2007; Jull & McKenzie, 1996; Maclennan et al., 2002; Sigmundsson et al., 2010; Sigvaldason et al., 1992). We compare our geochemical and mineralogical results of the intraglacial and interglacial volcanoes at the SAND-E 2019 catchment area to current hypotheses on glaciovolcanism and the geological history of the area. Finally, we will detail the mineralogical and geochemical characteristics of glaciovolcanism and hydrovolcanism that can be recognized by a Mars rover and orbiter to identify the signatures of glaciovolcanism and hydrovolcanism on Mars.

4.1. Geochemical and Mineralogical Characteristics of Glaciovolcanism

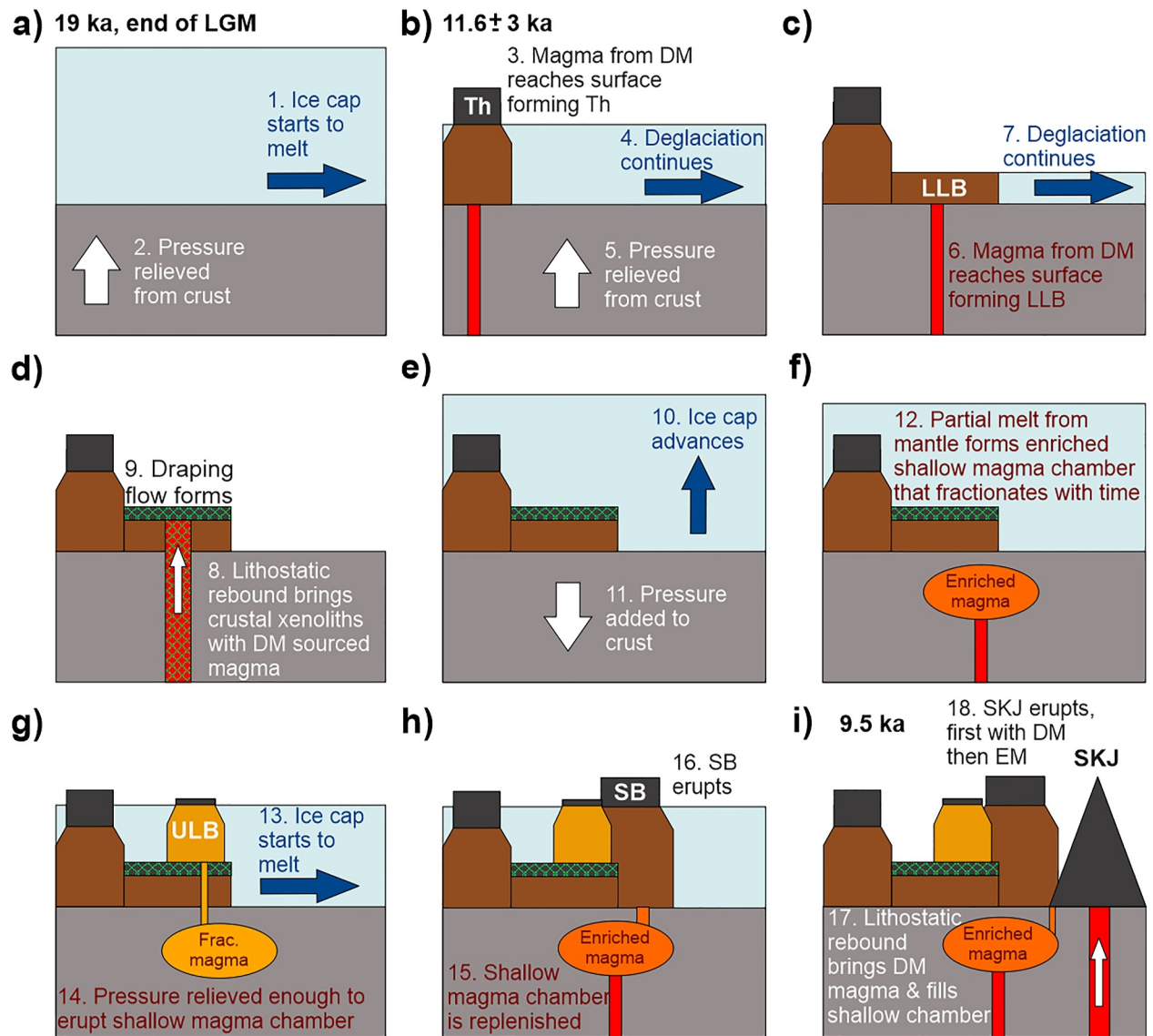
One of the main differences between intraglacial and interglacial volcanism in Iceland is the degree of quenching and fragmentation of the lava (e.g., Jakobsson & Gudmundsson, 2008; White, 2000). In Iceland, postglacial

volcanism usually results in thick lava flows that range from finely crystalline at the exterior part of the flow to coarsely crystalline at the interior part of the flow (Jakobsson et al., 1978; Sinton et al., 2005). In our samples, subaerial flows are largely crystalline with only 5.8 wt% average X-ray amorphous. This shows that the subaerial flows were not quenched and cooled slowly over time. On the other hand, as a volcano erupts through an ice sheet, it forms a melt pocket of water within the ice, which rapidly quenches the lava during an intraglacial eruption (M. T. Gudmundsson et al., 1997; Pedersen et al., 2020; Smellie, 2018). In the early stages of a glaciovolcanic eruption, it is more likely for pillow basalts to form due to the pressure from the overlying glacier suppressing the exsolution of volatiles from the lava (Höskuldsson et al., 2006; Sigvaldason, 1968). However, in the later stages of the eruption when the pressure is low, there is an increased chance of fragmentation and the formation of hyalotuff and pillow breccia (Jakobsson & Gudmundsson, 2008; van Otterloo et al., 2015).

Pillow lavas have a glassy selvage on the exterior where they are quenched but become more coarsely crystalline toward the center (Höskuldsson et al., 2006). Our results show that the amount of amorphous material varies for pillow morphologies from the interglacial volcanoes (0.0–33.3 wt%) depending on whether or not the glassy selvage was sampled. As such, X-ray amorphous abundance is not necessarily a good indicator for pillow basalts. Geochemically, XRF data from this study show that there is no difference between subglacial pillow and subaerial lava flow morphologies from the same volcanic source (Figure 9). Therefore, only a petrological and image analysis will be able to accurately identify subglacial pillow facies from subaerial lava flows. However, in this study, pillow basalts derive a relatively small volume of the intraglacial volcanoes (Figure 4), with most of the intraglacial volcano subglacial units consisting of the hyaloclastite and hyalotuff that form in the later stages of a subglacial eruption. As pillow basalt formation is enabled by higher pressures encouraging more effusive underwater eruptions (Höskuldsson et al., 2006; Sigvaldason, 1968), the lower atmospheric pressure and gravity on the surface of Mars may make it less likely for pillow basalt deposits to occur in hydrovolcanic assemblages. As such, the difficulties in identifying this morphology with rover-based techniques may be less relevant for Mars-based missions.

Our data show that hyaloclastite and hyalotuff have consistently high amorphous abundances with averages of 64.0 and 93.7 wt%, respectively (Figure 10). Hyaloclastite has a lower amorphous abundance as it can contain brecciated fragments of tachylite and phenocrysts from previous pillow units (Figure 7e). Hyalotuff investigated here has been well sorted and only contains the fragmented and rapidly quenched sideromelane glass grains (Figure 7c) with rare phenocryst phases showing quench textures such as skeletal olivine phenocrysts (Figures 7c and 7d). As such, we suggest that a high amorphous abundance at a candidate glaciovolcano on Mars can be attributed to a rapid quenching environment indicative of glaciovolcanism. This is consistent with the conclusions of an infrared spectroscopic study of tephra from hydrovolcanic eruptions containing a higher glass abundance (Henderson et al., 2021). Quench textures are difficult to identify in hand specimens, such as at the scale of a rover image; however, they are important indicators of an eruptive environment and can be looked for in returned samples from Mars using similar microprobe techniques as used in this study.

Palagonite and secondary alteration minerals such as phyllosilicates and iron oxides can also form in hyaloclastite and hyalotuff as fluids trapped in the pore spaces interact with the surrounding sideromelane grains (Figure 13) (Drief & Schiffman, 2004; Stroncik & Schmincke, 2001). XRD data of the SAND-E 2019 samples show that secondary alteration minerals are present as zeolites (chabazite or dawsonite), quartz, and clays (nontronite), however their abundances are not high (average of 1.1 wt% for hyaloclastite and 0.3 wt% for hyalotuff) relative to subaerial flows that have been exposed to precipitation and surface water runoff (e.g., SBCap02 has 2.5 wt% secondary mineral abundance, see Data Set S1). Secondary alteration minerals in the SAND-E 2019 hyaloclastite and hyalotuff are also not consistently present between samples, even from the same volcano. Previous studies have shown that the secondary mineral distribution in intraglacial volcanism is largely dependent on the alteration environment and height of the volcano (Bishop et al., 2002; N. H. Warner et al., 2010). Higher temperature zeolites (e.g., laumontite) are most common in the pillow basalts, pillow breccias, and hyaloclastites at the base of the volcano where glacial melt water has a greater interaction with larger lobes of lava that are able to retain more heat and release it over a longer timescale (Bishop et al., 2002; N. H. Warner et al., 2010). With more lava fragmentation higher up in the volcano, heat is more easily dispersed and lower temperature secondary alteration phases predominate (e.g., chabazite and smectite). In our samples, the main alteration product of the subglacial units is gel palagonite, which is included in the X-ray amorphous material of XRD data and cement the sideromelane, tachylite, and phenocryst grains (Figure 7). The mineralogy of palagonite is poorly defined and encompasses a wide range of chemical compositions, but previous research has shown that it forms at low



***Not to scale**

Figure 13. Conceptual model showing the evolution of Þórisjökull area as a response to climate-driven deglaciation with time based on field observations, geochemical, and mineralogical data. North is to the left of the image and South to the right. Dates are based on Eason et al. (2015). Magma ascent is illustrated as a red column for simplicity and represents the zone in which dykes may propagate from the mantle or magma chamber to the surface. The thickness of the red column represents the relative volume of ascending magma. (a) End of the Last Glacial Maximum, pressure starts to be relieved from the crust as the ice cap starts to melt. (b) Enough pressure has been released to allow magma from the depleted mantle source to erupt, forming Þórisjökull (Th). (c) Continued melting during the period of deglaciation allows more melt to reach the surface forming the Lower Litla-Björnsfell fissures. (d) Once the ice cap has retreated from this area, lithostatic rebound causes a large amount of melt to erupt from the depleted mantle source, bringing with it crustal xenoliths and forming the subaerial Draping Flow. (e) Another period of glaciation occurs, eroding the top of the Draping flow. (f) A shallow magma chamber forms with magma enriched in incompatible elements, likely through greater degrees of partial melting of the mantle. Shallow magma chambers are more likely to form at this stage as melt tries to make its way to the surface but is impeded by the overlying pressure of the ice cap. (g) Crystal fractionation occurs in the shallow magma chamber creating a more evolved composition that is then erupted as Upper Litla-Björnsfell (ULB) when the ice cap starts to melt. (h) As the pressure is relieved from the surface, this allows the shallow magma chamber to be replenished with melt and Stóra-Björnsfell erupts. (i) By 9.5 ka, the ice cap had retreated once more and melt is sourced from both the depleted mantle and enriched, shallow magma sources to form Skjaldbreiður.

temperatures (<100°C) over periods of less than 3 years (Jakobsson & Moore, 1986; Stronck & Schmincke, 2001, 2002). The zeolite chabazite-Ca exists in the hyaloclastite of Lower Litla-Björnsfell, which is also a low-temperature phase (<70°C) (Weisenberger & Selbekk, 2009; Wood et al., 1976), as is the nontronite that is usually present in chabazite-bearing samples for the SAND-E 2019 source rocks and in low-temperature hyalotuff in Hawai'i (Drief & Schiffman, 2004). Overall, the secondary alteration phases and abundant gel

palagonite support a low-temperature (<70°C) origin of the hydrothermal alteration in the SAND-E 2019 source intraglacial volcanoes. As the high-temperature assemblages usually exist toward the core of the volcano (N. H. Warner et al., 2010), it is possible that these phases were not exposed at the volcanoes in the SAND-E 2019 field site.

In this study, hyaloclastite and hyalotuff have distinct geochemical variations relative to the pillow and subaerial lava morphologies, showing consistently higher TiO₂, FeO_T, and MnO, and lower CaO, Na₂O, and V in XRF data (Figure 11). For our hyaloclastite samples that contain tachylite in addition to sideromelane, the palagonite that cement the grains has a composition indicative of the increase in FeO_T abundances relating to the alteration of olivine, a mixture of olivine and feldspar, and the alteration of glass (Figure 12). TiO₂ shows enrichment in the palagonite that appear to stem from the alteration of minerals and glass (Figure 12). As such, our results indicate that for hyaloclastite (Lower Litla-Björnsfell and Stóra-Björnsfell), palagonite cement can form from the interaction of pore fluids with mineral phases, particularly olivine, and groundmass phases (plagioclase and pyroxene) in microcrystalline tachylitic grains, not just from sideromelane glass. Previous research has shown that CaO and Na₂O are consistently leached from basaltic glass during palagonite evolution (Stroncik & Schmincke, 2001), and that immobile elements such as TiO₂ and FeO_T can become enriched in the palagonite cement (Drief & Schiffman, 2004). Our results agree and show that these elements can also be mobilized and enriched from the phenocryst and groundmass phases present in tachylitic grains.

Similar to the appearance of different secondary minerals not being consistent between samples, other geochemical variations in XRF data from this study are also present between hyaloclastite and hyalotuff samples, such as higher Al₂O₃ and Ba, and lower MgO, Ni, and Cr for Lower and Upper Litla-Björnsfell, which is not seen in Stóra-Björnsfell samples (Figure 11). Lower Litla-Björnsfell also shows a strong enrichment (up to 1.8x) in K₂O, which is depleted in Upper Litla-Björnsfell and Stóra-Björnsfell. The increase in K₂O for Lower Litla-Björnsfell palagonite is also shown in the sample microprobe data collected in this study, confirming that it relates to the formation of the palagonite cement (Figure 12). Palagonite has different compositions depending on the stage of palagonite evolution (Stroncik & Schmincke, 2001). Gel palagonite is characterized by the loss of Si, Al, Mg, Ca, Na, and K and enrichment of Ti and Fe. Most of the palagonite geochemical trends in the SAND-E 2019 source rocks relate to the gel palagonite stage, confirming the widespread detection of gel palagonite in the optical images (Figure 7). However, as palagonite ages with continued fluid interactions forming smectites, it can show an increase in Si, Al, Mg, and K as smectite removes these cations from the fluid (Stroncik & Schmincke, 2001). Sideromelane present in Upper Litla-Björnsfell is high in K₂O and the palagonite cement is low in K₂O (Figure 12). It is possible that K₂O has been remobilized from Upper Litla-Björnsfell and transported to Lower Litla-Björnsfell via percolating meteoric waters. The presence of zeolites and clays in Lower Litla-Björnsfell samples and absence of them from Upper Litla-Björnsfell samples further support the idea that Lower Litla-Björnsfell palagonite is likely more mature.

4.2. Deglaciation-Induced Changes in Magma Source and Renewed Geological History of the Area

A systematic variation in geochemistry associated with deglaciation has been recognized in volcanic rocks of the Reykjanes peninsula (Jakobsson et al., 1978), Western Volcanic Zone (Andrew & Gudmundsson, 2007; Eason et al., 2015; Jakobsson & Johnson, 2012; Sinton et al., 2005), and Northern Volcanic Zone (MacLennan et al., 2002) in Iceland. These systematic variations in geochemistry show a transition from high-MgO picritic lava with exceptionally low incompatible elements to olivine tholeiite, tholeiite and, in some rare occasions, rhyolite with high incompatible element abundances (Andrew & Gudmundsson, 2007; Eason et al., 2015; MacLennan et al., 2002; McGarvie et al., 2007). Several hypotheses exist to explain the geochemical changes associated with deglaciation, all of which relate the loss of ice from the surface with lithostatic rebound and enhanced decompression melting at various stages within the crust. Geophysical models showed that deglaciation of a ~2 km thick glacier, such as that hypothesized for the Last Glacial Maximum in Iceland, enhances melt production in the shallow mantle (60 km depth) (Jull & McKenzie, 1996; MacLennan et al., 2002). Furthermore, the additional weight on the crust from glaciation in the Last Glacial Maximum encouraged the formation of shallow magma chambers and suppressed volcanism until deglaciation began (Andrew & Gudmundsson, 2007; Jull & McKenzie, 1996). According to Andrew and Gudmundsson (2007), in the early stages of deglaciation, pressure is first relieved from the deeper source in the mantle, producing picritic melts with low incompatible trace element abundances. Next, the less dense olivine tholeiite melts dominate the eruptions of the deeper magma source in the mantle. Finally, once the ice caps have melted and sufficient pressure has been released from the

crust, the shallow magma chambers erupt their fractionated more evolved lava that can extend to rhyolitic compositions (McGarvie et al., 2007). Previous geochemical studies of the WVZ that include our field locality support hypotheses relating to the geophysical models but suggest that deglaciation-induced melting occurred earlier than hypothesized by the geophysical studies (Eason et al., 2015). In this section, we discuss how our geochemical and mineralogical data for non-tuff volcanic units in the Þórisjökull locality of SW Iceland relate to previous hypotheses of deglaciation induced melting in the region.

Our geochemical results of the non-hyaloclastite units showed that the volcanoes in our area can be grouped into five clusters, three of which (Cluster 1, 3, and 5) can fit within these systematic regional trends (Figure 9). Subglacial units and lava within Cluster 1 have low TiO_2 , FeO_T , K_2O , P_2O_5 , and high CaO, similar to “chemical group A” from Eason et al. (2015) and other early post-glacial lava around Iceland, such as those from Theistareykir and Krafla (MacLennan et al., 2002). The low abundances of incompatible elements (TiO_2 , P_2O_5 , Zr, Sr, Ba) of this chemical group are hypothesized to be the result of a greater volume of melt generated in the shallow part of the mantle (Eason et al., 2015; MacLennan et al., 2002). The higher SiO_2 , CaO, and lower FeO_T abundances of the lava in Cluster 1 (or chemical group A) are also consistent with enhanced decompression melting of a peridotite mantle source, similar to that in the uppermost mantle below Iceland (Eason et al., 2015; MacLennan et al., 2002). From our results, both Lower Litla-Björnsfell and Þórisjökull are classified within this cluster, indicating that not only did both volcanoes likely stem from mantle-derived melts but also likely formed around the same point in the glacial-interglacial cycle in the early stages of deglaciation. Eason et al. (2015) determined the exposure ages of Þórisjökull to be 11.6 ± 0.3 ka, forming toward the end of the Younger Dryas and likely erupting through a significant ice sheet. Based on the superposition relationship between the capping lava of Lower Litla-Björnsfell and Þórisjökull from our satellite mapping, Lower Litla-Björnsfell most likely formed not long after Þórisjökull. However, the difference in Passage Zone height from 300 m for Þórisjökull and 100 m for lower Litla-Björnsfell indicates that the incompatible element depletion continued during significant ice loss and continued through the eruption of the subaerial Draping Flow.

Clusters 2 and 4 show extremes in composition with extremely high MgO correlating to an enrichment in olivine for Cluster 2 samples and high Al_2O_3 and CaO correlating to high feldspar abundances for Cluster 4 samples. This suggests that Clusters 2 and 4 are likely cumulates with incompatible element abundances making them most similar to Cluster 1 and henceforth most likely to be derived from a similar magmatic source. The subaerial Draping Flow overlying Lower Litla-Björnsfell also contains gabbroic nodules with extremely high MgO abundances correlating with high olivine abundances (Figure 6a). These nodules are coarsely crystalline, with olivine and pyroxene minerals up to 1 cm in size and feldspar minerals inhabiting the intragranular spaces (Figures 6b and 6c). Several olivine crystals have a sieve texture and rims with lower Mg# numbers than their cores (Figure 6c), suggesting that they were not in equilibrium with the melt they were emplaced within during the eruption. Furthermore, the olivine minerals in the Draping Flow have a far greater range in Mg# values than that of the olivine phenocrysts in Lower Litla-Björnsfell, which in turn have the most forsteritic compositions of the olivine phenocrysts in the area. Previous research on olivine macrocrysts and gabbro nodules entrained within Icelandic basalts has shown that the olivine minerals span a wide range in composition and are often in disequilibrium with their carrier liquid (Einarsson et al., 2013; Gurenko & Sobolev, 2006; Tronnes, 1990). It is possible that these olivine macrocrysts may represent olivine accumulation in a shallow magma chamber that was then entrained after the magma chamber was replenished and later erupted as the Draping Flow. However, an isotopic study of olivine macrocrysts from another volcano on the Reykjanes Peninsula, Hengill, shows that their Sr isotope values more closely match those of the Icelandic crust (Einarsson et al., 2013). As such, it is likely that these olivine macrocrysts have been derived from interactions of an ascending magma with the thick Icelandic crust that, similarly to ophiolites, contains layered gabbros. Layers of pure plagioclase can be observed to exist within layered gabbro complexes in ophiolites (Boudier & Nicolas, 2011; Sotiriou & Polat, 2020). These could also be a source of the felsic rock found at the base of Þórisjökull, which derives the high Al_2O_3 Cluster 4. Therefore, these gabbro nodules and feldspar cumulates in the Draping Flow and Þórisjökull volcano are also likely to be a product of magmatism from the early stages of deglaciation, as mantle overpressure is enhanced and the likelihood of crustal fragments to be entrained during their ascent is increased at this time (Einarsson et al., 2013; Tronnes, 1990).

Clusters 3 and 5 are most similar to one another in the Cluster analysis (Figure 9) and are similar to Chemical Groups B and C from Eason et al. (2015), respectively. Clusters 3 and 5 have moderately high to high incompatible elements such as TiO_2 , K_2O , P_2O_5 , slightly higher FeO, and lower CaO than those of Cluster 1. Chemical

Groups B and C from Eason et al. (2015) have trace element abundances that are within the expected range for normal melting models of the mantle underlying Iceland; as such, it is likely that these volcanoes did not erupt during a stage of rapid deglaciation. Volcanoes belonging to Cluster 3 include Stóra-Björnsfell and Skjaldbreiður. Stóra-Björnsfell erupted prior to significant ice loss based on its high Passage Zone height (450 m) implying a thick ice cap (Eason et al., 2015), and Skjaldbreiður is a postglacial shield volcano with a large, erupted volume (15 km³, Sinton et al., 2005). Both Stóra-Björnsfell and Skjaldbreiður have glomerocrysts of plagioclase feldspar, clinopyroxene, and olivine, suggesting that their magmas crystallized in a shallow crustal reservoir at the cotectic of these mineral phases (Jakobsson et al., 1978). The formation of shallow magma chambers beneath calderas and central volcanoes is common in Iceland (A. Gudmundsson, 1995), and geophysical modeling suggests that glaciation encourages the formation of shallow magma chambers (Andrew & Gudmundsson, 2007). It is possible that smaller volumes of magma with higher degrees of partial melting and therefore higher abundances of incompatible elements collected in a shallow magma chamber, crystallizing the glomerocrysts that then erupted Stóra-Björnsfell, and later Skjaldbreiður.

The lavas that form Cluster 5 belong to Upper Litla-Björnsfell, which have slightly more incompatible trace elements than Stóra-Björnsfell and Skjaldbreiður and have a more evolved chemical composition that lies along a fractional crystallization trendline from the lava of Cluster 3 (Stóra-Björnsfell and Skjaldbreiður). This suggests that the lavas that formed Upper Litla-Björnsfell were from a source similar to that of Stóra-Björnsfell and Skjaldbreiður but had undergone more fractional crystallization. Based on field relationships, it is unclear which volcano erupted first. The passage zone sequence of Stóra-Björnsfell occurs at a height similar to the thin sub-aerial lava cap of West Upper Litla-Björnsfell (~400 masl). Fractional crystallization is most likely to occur prior to the initiation of deglaciation (Andrew & Gudmundsson, 2007), suggesting that Upper Litla-Björnsfell erupted at the initiation of deglaciation. Then, the shallow chamber may have been replenished with magma and Stóra-Björnsfell erupted shortly after without undergoing much fractional crystallization (Figure 13). Once the ice had retreated from this area, Skjaldbreiður erupted. Older units of Skjaldbreiður are exposed to the W and SW of the SAND-E 2019 field site and have been shown to have low incompatible element abundances, but the parent magma of Skjaldbreiður changed to a more enriched source as the eruption progressed (Sinton et al., 2005), suggesting that this shield volcano perhaps tapped into both the deeper mantle source and shallow crustal source of Stóra-Björnsfell during its long eruptive history.

Overall, placing our results in the context of existing models on the impact of glaciation and deglaciation on Icelandic volcanism has allowed us to constrain the geological history of our field site (Figure 13). The first volcanism to have occurred at the Last Glacial Maximum was likely the eruptions that created Þórisjökull. Þórisjökull has significant incompatible element depletions, and the high CaO abundances indicative of a depleted mantle source and also contains crustal xenoliths. Þórisjökull's Passage Zone height is estimated to be at 300 m and has an exposure age of 11.6 ± 0.3 ka (Eason et al., 2015), which suggests a thinner ice cap than the thickness of ice at Langjökull (up to 650 m in 2007, (Pope et al. 2016)), the neighboring ice cap to Þórisjökull. Lower Litla-Björnsfell has a similar chemistry to Þórisjökull suggesting that these fissure eruptions occurred at a similar time and from a similar source to Þórisjökull. The rapid deglaciation continued until the subaerial Draping Flow erupted over Lower Litla-Björnsfell and a significant area to the West of the SAND-E field site, carrying with it crustal xenoliths of olivine cumulates. After this period of rapid deglaciation, there was likely another period of glacier advancement, causing glacial smoothing and striations on the Draping Flow. This glaciation was substantial, with an ice cap thickness exceeding 450 m and suppressed magmatism enough for fractional crystallization to have occurred in a shallow magma chamber. Next, during the early stages of deglaciation, Upper Litla-Björnsfell erupted, barely reaching the top of the ice cap, and forming high TiO₂ and K₂O lava and hyalotuff. After this, Stóra-Björnsfell may have formed after further deglaciation and the recharge of the shallow magma chamber. Then, once the ice cap had fully retreated from the area, Skjaldbreiður erupted with a lithostatic rebound following deglaciation, sampling both the depleted mantle and shallow crustal sources, including those which contributed to Stóra-Björnsfell.

5. Mars Implications

From thoroughly investigating the impact of glaciovolcanism on the geochemistry and mineralogy of Iceland's volcanic rocks, it is evident that not only can the presence of a thick ice cap impact the morphology of the erupted products and shape of the volcanoes, but also the geochemistry and mineralogy of the magma itself. It is likely that glaciovolcanism would also impact the geochemistry and mineralogy of deposits on Mars, but due to Mars having

a lower gravity (~38% that of the Earth's) and lower present day atmospheric pressure (<1% that of the Earth's) there are likely to be differences.

5.1. The Effect of Different Planetary Environments on Glaciovolcanic Units

Water ice is currently present on Mars at the polar ice caps and in high-latitude permafrost (Byrne, 2009; Clifford et al., 2000; Feldman et al., 2004). The distribution of candidate glaciovolcanic landforms on Mars (Figure 2), in addition to other features identified from orbital imaging associated with glaciation at high- and mid-latitudes such as eskers (e.g., Butcher et al., 2016, 2017; Grau Galofre et al., 2022; Souness & Hubbard, 2012), suggests that the distribution of water ice deposits has varied across Mars with time, likely driven by Mars' large changes in obliquity (Clifford et al., 2000; Jakosky et al., 1995; Levrard et al., 2004). Liquid water is not stable at Mars' current atmospheric pressure. However, there is a wealth of evidence such as river channels, delta fans, and hydrated minerals detected from orbit and investigated in situ with rovers, which shows that in the past, liquid water was able to shape the landscape, filling crater lakes and possibly even forming an ocean in the Northern hemisphere (M. H. Carr & Head, 2010; Ehlmann et al., 2009; Grotzinger et al., 2015; B. H. N. Horgan et al., 2020; Rampe et al., 2020). This shows that despite Mars' current cold and dry conditions, enough water has been present on Mars' surface throughout time to suggest that the atmosphere was likely thicker than it is today. As such, it is possible for hydrovolcanic and glaciovolcanic landforms to have formed throughout Mars' geological history.

Pressure plays an important role in the formation of glaciovolcanic morphologies as high pressures suppress magma-water interactions and inhibit the exsolution of magmatic gases, reducing the likelihood of explosivity and encouraging the formation of pillow lava (Sigvaldason, 1968; Sigvaldason et al., 1992; Zimanowski & Buttner, 2003). Pillow lava can form in shallow water environments when the flow rate is low, such as in lava delta sequences (e.g., Le Masurier, 2002); however, these deposits are usually brecciated due to the increased likelihood of explosivity at low pressures, often enhanced by wave-generated turbulence or brecciation during downslope movement. The lower gravity and atmospheric pressure of Mars is hypothesized to increase the explosivity of Martian eruptions, particularly in the Noachian and Hesperian when volatile abundances were likely higher and/or there was a greater availability of surface water (Brož et al., 2021; Leone, 2021). To conduct a quick planetary comparison, a simple one-dimensional model is employed for the purpose of this discussion. The main volatiles in basaltic melts that are degassed during an eruption are CO₂, S, and H₂O. As CO₂ is much less soluble in a silicate melt compared to the other volatiles and degasses at depth in the crust, H₂O is the most abundant volatile at lower pressures and is more relevant when calculating the pressure required to form pillow basalt in subglacial eruptions (Höskuldsson et al., 2006; Sigvaldason, 1968). The current concentrations of volatiles in ascending magmas on Mars are poorly constrained and expected to have varied through time with some studies calculating up to 2 wt% H₂O present before eruption and others hypothesizing that Mars magmas are essentially anhydrous (Filiberto et al., 2016). To calculate the relative thickness of ice or water required to suppress significant volatile release from a basaltic melt on the Earth and Mars, we take the maximum pressure of water saturation at the point of fragmentation in the relatively anhydrous (0.45 ± 0.03 wt% H₂O) lava erupted from the 2,500 ka phreatomagmatic Hverfjall fires (E. J. Liu et al., 2018) P_{H₂O} = 2.6 MPa and apply it to the equation:

$$h = \frac{P_{\text{H}_2\text{O}} - P_0}{\rho g} \quad (1)$$

where h is the thickness of the water or ice, P_0 is the atmospheric pressure at sea level on the Earth (0.1 MPa) or at the mean radius of Mars (636 Pa), ρ is the density of ice ($9.17 \times 10^2 \text{ kg/m}^3$) or water at 4°C ($1 \times 10^3 \text{ kg/m}^3$).

Based on our simplistic model, water saturation in a lava is reached with an ice thickness of 277 m on the Earth compared to 760 m on present-day Mars, whereby a reduction in ice load will result in an exponential release of water as gas (Figure 14). The results for the required height of a column of water are similar to 254 m of water required to suppress H₂O exsolution on the Earth and 697 m of water needed for present-day Mars. Differences in atmospheric pressure on Mars between present-day conditions and an Earth-like atmospheric pressure only contribute a 3.9% difference in the thickness of a column of water or ice required to suppress vesiculation (Figure 14). The results of this model reasonably fit our field observations in Iceland where we see pillow basalt units up to 150 m in Stóra-Björnsfell and have an estimated ice cap thickness of 400–450 m requiring about 250–300 m of ice cap to form thick pillow deposits (Figure 4). If Stóra-Björnsfell erupted on Mars, it would require an ice sheet of over 800 m to form substantial basal pillow lava deposits. Candidate glaciovolcanoes on Mars

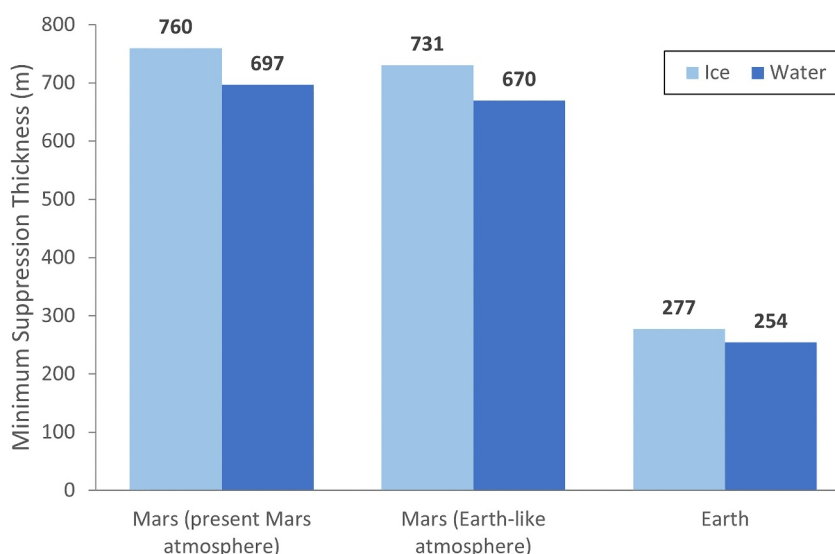


Figure 14. Calculated minimum ice and water thicknesses required to suppress significant fragmentation from a Icelandic lava if it erupted on the Earth or on Mars. Thicknesses are calculated from Equation 1. As a comparison between ancient Mars where atmospheric pressure was sufficient to sustain liquid water at the surface, and present-day Mars, minimum ice and water thicknesses were also calculated with Mars gravity and Earth atmospheric pressure at sea level (or mean radius of Mars).

exhibiting a Tuya-like morphology have a wide range of heights ranging from 100 m to several km thick (C. Allen, 1979; Chapman & Tanaka, 2002; Ghatan & Head, 2002; Martínez-Alonso et al., 2011). It is difficult to identify a passage zone sequence from orbital data, so we use these heights as a first order estimation of ice thickness. Overall, the Acidalia Planitia candidate glaciovolcanoes have a maximum height of 500 m (Martínez-Alonso et al., 2011), which may not have been sufficient to produce thick deposits of pillow basalts at the base unless the magmas that produced them had an even lower volatile budget than the modeled example used here. However, candidate glaciovolcanoes present at the South Polar region of Mars have a height of 1,000–1,500 m (Ghatan & Head, 2002), which indicates a sufficient ice cap thickness to produce the pressure required for large pillow basalt deposits such as those seen at the base of large Icelandic glaciovolcanoes.

In Iceland, hyaloclastite and hyalotuff are the most abundant morphologies in glaciovolcanoes, deriving approximately 50% of the volume of the volcano. The results of our simple numerical model suggest that Mars hydrovolcanism would favor more explosive eruption styles, supporting the conclusions of previous studies investigating volcanism on Mars (Brož et al., 2021; Horvath et al., 2021; Moitra et al., 2021). As such, the weakly consolidated glass-rich hydroclastic deposits known as hyaloclastite and hyalotuff would likely be an even greater contributor to glaciovolcanic edifices on Mars. The image resolution and dust cover on Mars from orbital data make it difficult to resolve the morphologies of candidate glaciovolcanoes; however, our results and those from previous studies show that these units have unique chemical and mineralogical signatures. Due to the high abundance of glass (>50 wt% hyaloclastite and >90 wt% hyalotuff) and their formation requiring the interaction of water, these morphologies also contain varying abundances of palagonite and secondary alteration minerals dependent on their location within the glaciovolcano. Such minerals that are likely to be formed by the aqueous alteration of glaciovolcanic-derived palagonite include smectite and Fe-oxides/oxyhydroxides (Pandey et al., 2023). Mineralogical investigations from the orbit of the candidate glaciovolcanoes on Mars have been scarce. However, weathered glass and Mg-smectites have been identified from orbit in the Siton Undae and Acidalia Planitia regions of the northern lowlands using OMEGA data (B. Horgan & Bell, 2012; Martínez-Alonso et al., 2011). B. Horgan and Bell (2012) speculate the glass formed from explosive subglacial volcanism based on spectra consistent with iron-bearing glass sand grains of low vesicularity, which, in combination with the candidate glaciovolcanic features, provides a strong case for glaciovolcanism in this area. Those in Sisyphi Planum contain smectite, zeolite, and iron oxides hypothesized to represent palagonite (Ackiss et al., 2018), supporting their likelihood of being Martian glaciovolcanoes.

In addition to these geochemical changes relating to the formation of the hyaloclastite and hyalotuff, our results support that glaciation encourages the formation of shallow magma chambers and that the rate of glaciation

impacts where the magma is sourced. Areas that likely experienced glaciovolcanism should exhibit a diversity of igneous minerals with extensive fractional crystallization present in volcanoes that have erupted from shallow magma chambers that were suppressed from erupting due to the long-standing presence of a thick ice cap. They should also show variations in incompatible element concentrations for basaltic melts, indicating different degrees of partial melting between periods of glaciation and deglaciation. Due to the difficulties in detecting feldspar with VNIR spectroscopic methods, orbital detections of evolved magma compositions have been rarely reported and heavily debated for Mars. However, rocks with mineral compositions indicative of changes in magma source including an evolved magma composition indicative of rhyolite have also been detected in Gale crater (Bowden et al., 2023; Cousin et al., 2017; Edwards et al., 2017; Morris et al., 2016; Sautter et al., 2014; Treiman et al., 2016). It is possible that crustal loading by glaciation could be a contributor to forming these evolved igneous assemblages on a planet without plate tectonism.

5.2. Detecting Glaciovolcanism in the Mars Sedimentary Record

Mars' planetary surface has experienced extensive reworking of volcanic deposits using sedimentary processes. Rovers are typically sent to areas where geomorphological observations indicate that sediments were likely deposited by wind-blown processes, rivers, and lakes; therefore, rovers may encounter sediments eroded from glaciovolcanic igneous deposits rather than the igneous deposits themselves. Indeed, the CheMin X-ray diffractometer on the Curiosity rover has identified abundant X-ray amorphous materials (~20–70 wt.%) in all sedimentary rocks analyzed to date (Rampe et al., 2020). A study by Wall et al. (2014) based on CheMin XRD results of the lacustrine basaltic sediments and aeolian sand shadow at Yellowknife Bay suggests a pyroclastic origin for Gale crater's amorphous-rich sediments. However, post-depositional aqueous alteration obscures whether or not this could relate to phreatomagmatism such as that occurs during glaciovolcanism. Mass-balance calculations using APXS data show that these amorphous materials in Gale crater's sediments vary in composition between an FeO_T-rich endmember and a SiO₂-rich endmember (Smith et al., 2021), with increasing SiO₂ content hypothesized to relate to increased post-depositional aqueous alteration or changes in sediment provenance. Based on our geochemical and mineralogical measurements of glaciovolcanic deposits in Iceland, glaciovolcanic sediments may be recognized on Mars through the identification of high abundances of X-ray amorphous materials and at least a 10% increase in TiO₂, >5% increase in FeO_T, >5% increase in MnO, and a strong decrease in CaO (10%–20%), Na₂O (10%–30%) and V (10%–30%) relative to unaltered volcanic glass from the same volcano. As such, an FeO_T-rich amorphous endmember is consistent with the formation of palagonite during a subglacial eruption within the hyaloclastite and hyalotuff units.

Studies of the maturation of palagonite suggests that additional chemical weathering and aqueous alteration would further increase the TiO₂ and FeO_T abundances relative to those of more mobile elements for the palagonite component of these materials (Bell et al., 1993; Stroncik & Schmincke, 2001), but presently there are limited studies investigating the evolution of glaciovolcanically derived palagonite during transportation in fluvio-lacustrine or aeolian systems relevant to Mars. N. H. Warner and Farmer (2010) showed that the secondary alteration features and overall characteristics of hyaloclastite and hyalotuff can be preserved in the catastrophic flood deposits caused by glaciovolcanism; however, mineralogical investigations of the aeolian sand sheets that rework these deposits show that secondary alteration minerals are scarce (Baratoux et al., 2011). This is likely a factor of physical weathering processes during aeolian transportation removing the relatively soft palagonite cement of hyaloclastite and hyalotuff deposits, winnowing them away as wind, while the more physically resilient glass is transported and concentrated in the coarser grain size fractions (Cornwall et al., 2015). VNIR spectroscopy studies of glaciovolcanic palagonite have also shown a similarity to the palagonite in Iceland's glaciovolcanoes and the palagonitic dust on Mars investigated with the Viking landers, suggesting that glaciovolcanism, or hydrovolcanism in general, could be a possible source of widespread palagonite in Mars' dust (Bell et al., 1993; Bishop et al., 2002).

In general, there are several possible geochemical and mineralogical indicators of glaciovolcanism in Mars' sedimentary deposits, particularly in the Gale crater. However, it is important to note that the hyaloclastite and hyalotuff which form in a glaciovolcano can also form in other hydrovolcanic settings (e.g., eruption into an ocean or lake). As such, unless there is a candidate glaciovolcanic edifice in the watershed of the Martian field site that formed around the same time as the sedimentary deposits under investigation, it is difficult to distinguish from the sediments alone what type of hydrovolcanic environment they erupted into. Additional geochemical or mineralogical differences that could occur from volcanoes erupting through a glacier versus erupting into a lake or

ocean are diversity in igneous compositions that can be driven by glacial-interglacial cycles but not from the presence of a standing body of water. As mentioned previously, Gale crater's geological record does contain geochemical and mineralogical variations indicative of multiple igneous sources (Bedford et al., 2019; Berger et al., 2020; Payré et al., 2020), possibly related by different degrees of fractional crystallization from a basaltic magma (Payer et al., 2020; Udry et al., 2018). Although some of these more evolved igneous sources are coarsely crystalline like the trachybasaltic source present in the float and conglomerates of the crater floor (Bedford et al., 2019; Edwards et al., 2017) or the Askival feldspathic cumulate (Bowden et al., 2023), suggesting that not every sedimentary source in Gale crater has a possible hydrovolcanic origin.

5.3. Identifying the Products of Glaciovolcanism and Hydrovolcanism With Mars Sample Return

With the Perseverance rover currently collecting and caching samples in Jezero crater for their return to the Earth with the Mars Sample Return mission, it is likely that we will be able to perform in situ analyses of Mars igneous and sedimentary samples in the laboratory as soon as 2031 (Muirhead et al., 2020). The main goal of the Mars 2020 mission is to locate and characterize rocks in Jezero crater that hold the greatest potential of preserving ancient Martian life (Farley et al., 2020). Other goals of sample collection include targeting geological samples that can constrain the geological record of Mars and the history of Martian volatiles throughout time. Based on these constraints, hydrovolcanically derived materials would be of great interest given their implications for the presence of water or ice during their formation and ability to retain volatiles in melt inclusions. Glaciovolcanism in particular has also been shown to support bacterial communities in hydrothermal systems, with the high glass and palagonitic nature of most of these deposits proving particularly susceptible to biological and chemical weathering (Cockell et al., 2009; Cousins, 2015; Kelly et al., 2010; Ryan et al., 2024). This is because chemolithoautotrophic bacteria are more readily able to access the elements required for their metabolism in the metastable glass and palagonitic products. Furthermore, glaciovolcanism is able to sustain englacial, subglacial, or proglacial environments between and during eruptions for oligotrophic microbial communities to thrive (Cockell et al., 2009; Cousins, 2015; Kelly et al., 2010). Jezero crater has been selected as the landing site for the Perseverance rover based on geomorphological and mineralogical studies from orbit suggesting a long-lived fluviolacustrine environment occurring (Farley et al., 2020; B. H. N. Horgan et al., 2020).

Since landing, the Perseverance rover has explored a crater floor containing igneous units and a sedimentary delta-fan. A geological history of igneous and lacustrine processes makes it possible for hydrovolcanism to have occurred within the Jezero crater itself and the nearby Syrtis Major volcanic province contains units mapped from orbit as potentially relating to explosive volcanism (e.g., Fawdon et al., 2015). Despite the implications for a long-lived lake environment, the igneous units of the Jezero crater floor are overall coarsely crystalline and have textures indicative of cumulate rocks or subaerial lava flows (Alwmark et al., 2023; Y. Liu et al., 2022; Udry et al., 2023), however, laterally continuous, recessive, thin layers of friable material exist, which could represent hyaloclastite deposits from lava entering a lake environment (Alwmark et al., 2023). This suggests that either detrital or in situ hydrovolcanic deposits, if not glaciovolcanic, are possible in Jezero crater. The Perseverance rover instrument suite is not able to easily identify volcanic glass and palagonite in geological samples as mineralogical characterization is dependent on VNIR spectroscopy with the Mastcam-Z and SuperCam instruments in which basaltic glass is spectrally flat. Geochemical data provided by laser-induced breakdown spectroscopy with the SuperCam instrument and element mapping with micro-XRF do not provide information on crystallinity. As such, identification would have to heavily rely on close-up images acquired with the rover by the WATSON and SuperCam images (e.g., glass inferred texturally by Udry et al. (2023)). Table 2 includes ways to identify the products of hydrovolcanism in rover-based Mastcam-Z and close-up images. Upon return to the Earth, petrographic indications of hydrovolcanism include looking for quench textures, such as dendritic feldspars or hollow olivine grains within a sideromelane or plumose feldspar and pyroxene groundmass, which can be corroborated with XRD analyses, SEM studies to look for signs of biological weathering, and microprobe studies to investigate the volatile content of trapped melt inclusions and aqueous alteration conditions of the glass grains.

6. Conclusions

To conclude, glacial-interglacial cycles can have a noticeable impact on the morphology, chemistry, and mineralogy of igneous deposits on the Earth and Mars that can be detectable by instruments carried by orbiting spacecraft, rovers, landers, and in returned samples. As such, it is possible for volcanic edifices and their eroded products to be used as paleoenvironmental indicators when constraining Mars geological history.

In our Mars-analog investigation of Iceland, volcanism occurring after the initiation of deglaciation from the Last Glacial Maximum formed a large proportion of glass- and palagonite-rich hyaloclastite and hyalotuff deposits. These hyaloclastite and hyalotuff deposits are the most geochemically and mineralogically distinctive deposits relating to glaciovolcanism with a high X-ray amorphous abundance (up to 98 wt%), an increase in TiO₂, FeO_T, and MnO, and a strong decrease in CaO, Na₂O, and V relative to unaltered volcanic glass from the same volcano. At the scale of the outcrop and in hand specimens, these hyaloclastite and hyalotuff deposits can exhibit different degrees of sorting, grading, and soft-sediment deformation within beds of mostly ash and lapilli. Within thin section images, petrological evidence of quenching can be observed through quench textures such as skeletal primary igneous phases and abundant sideromelane. Hyaloclastite and hyalotuff grains are also cemented by poorly crystalline palagonite, smectites, and zeolites that are derived from the low-temperature alteration of glass and mineral phases with water during the eruption of these deposits. Fragmentation of sideromelane, tachylite, or mineral grains is also common during the eruption of hyaloclastite and hyalotuff, with some rounding occurring as the hyaloclastite and hyalotuff is transported downslope. Based on different planetary surface conditions between the Earth and Mars, Mars is more likely to have a greater contribution of these hyaloclastite and hyalotuff units in the formation of a glaciovolcano as the lower gravity and atmospheric pressure promote greater explosivity.

The results of our research in Iceland also support that glaciation likely suppresses magmatism from occurring, promoting the formation of shallow magma chambers that can fractionate to form more evolved compositions. The Þórisjökull field site also had volcanoes derived from two main magma sources: a depleted shallow mantle source and an enriched crustal source. The oldest volcanoes in the field site (Þórisjökull and Lower Litla-Björnsfell) were derived from the depleted shallow mantle source, while the younger volcanoes (Upper Litla-Björnsfell, Stóra-Björnsfell, and Skjaldbreiður) were likely sourced from the shallower enriched magma chamber. These geochemical and mineralogical variations between volcanoes in the field site along with field observations enabled us to constrain the geological history of this area and support the hypothesis that deglaciation can cause a systematic variation in geochemistry associated with different magma sources.

Conflict of Interest

The authors declare no conflicts of interest relevant to this study.

Data Availability Statement

Data types used in this manuscript include bulk geochemical data acquired by portable and benchtop XRF, mineralogical data acquired by XRD and refined using Profex 5.2.0 (c) 2003–2023 by Nicola Döbelin, and EMPA chemical data. The benchtop XRF data was also processed using the Minitab® 20.4 (64-bit) statistical software. Data used in this manuscript has been made available in the supplementary materials and has been archived in an online repository (Bedford, 2024 [Dataset]).

Acknowledgments

C. C. Bedford would like to acknowledge the NASA PSTAR program Grant 80NSSC18K1519 and the Lunar and Planetary Institute for funding during this research. The Authors thank the Icelandic government and Arctic Trucks for their support in conducting this research, in addition to N. C. Jopek for providing field assistance. C. C. Bedford would also like to acknowledge the staff at the NASA Johnson Space center for their support in acquiring and analyzing the data used in this research. In particular, Dr. Valerie Tu for their assistance in acquiring and analyzing the XRD data, Dr. Anne Peslier, Dr. Loan Lee, and Dr. Jennifer Gorce for their assistance in acquiring and interpreting the EPMA data, and Dr. Timmons Ericksson for assisting in the sample preparation.

References

- Ackiss, S., Horgan, B., Seelos, F., Farrand, W., & Wray, J. (2018). Mineralogic evidence for subglacial volcanism in the Sisyphi Montes region of Mars. *Icarus*, 311, 357–370. <https://doi.org/10.1016/J.ICARUS.2018.03.026>
- Allen, C. (1979). Volcano-ice interactions on Mars. *Journal of Geophysical Research*, 84(B14), 8048–8059. <https://doi.org/10.1029/JB084iB14p08048>
- Allen, C., Gooding, J. L., Jercinovic, M., & Keil, K. (1981). Altered basaltic glass: A terrestrial analog to the soil of Mars. *Icarus*, 45(2), 347–369. [https://doi.org/10.1016/0019-1035\(81\)90040-3](https://doi.org/10.1016/0019-1035(81)90040-3)
- Allen, R. M., Nolet, G., Morgan, W. J., Vogfjörð, K., Bergsson, B. H., Erlendsson, P., et al. (1999). The thin hot plume beneath Iceland. *Geophysical Journal International*, 137(1), 51–63. <https://doi.org/10.1046/J.1365-246X.1999.00753.X>
- Allen, R. M., Nolet, G., Morgan, W. J., Vogfjörð, K., Nettles, M., Ekström, G., et al. (2002). Plume-driven plumbing and crustal formation in Iceland. *Journal of Geophysical Research*, 107(B8), ESE4-1–ESE4-19. <https://doi.org/10.1029/2001JB000584>
- Alwmark, S., Horgan, B., Udry, A., Bechtold, A., Fagents, S., Ravanis, E., et al. (2023). Diverse lava flow morphologies in the stratigraphy of the Jezero crater floor. *Journal of Geophysical Research: Planets*, 128(7), e2022JE007446. <https://doi.org/10.1029/2022JE007446>
- Andrew, R. E. B., & Gudmundsson, A. (2007). Distribution, structure, and formation of Holocene lava shields in Iceland. *Journal of Volcanology and Geothermal Research*, 168(1–4), 137–154. <https://doi.org/10.1016/J.JVOLGEORES.2007.08.011>
- Baker, V. R., Strom, R. G., Gulick, V. C., Kargel, J. S., Komatsu, G., & Kale, V. S. (1991). Ancient oceans, ice sheets and the hydrological cycle on Mars. *Nature*, 352(6336), 589–594. <https://doi.org/10.1038/352589a0>
- Baratoux, D., Mangold, N., Arnalds, O., Bardintzeff, J.-M., Platevoët, B., Grégoire, M., & Pinet, P. (2011). Volcanic sands of Iceland—diverse origins of aeolian sand deposits revealed at Dyngjúsandur and Lambhraun. *Earth Surface Processes and Landforms*, 36(13), 1789–1808. <https://doi.org/10.1002/esp.2201>
- Bedford, C. C. (2024). Geochemical and mineralogical data of the Þórisjökull field site, Iceland [Dataset]. <https://doi.org/10.4231/FR4M-PF07>

- Bedford, C. C., Bridges, J. C., Schwenzer, S. P., Wiens, R. C., Rampe, E. B., Frydenvang, J., & Gasda, P. J. (2019). Alteration trends and geochemical source region characteristics preserved in the fluvio-lacustrine sedimentary record of Gale crater, Mars. *Geochimica et Cosmochimica Acta*, 246, 234–266. <https://doi.org/10.1016/j.gca.2018.11.031>
- Bedford, C. C., Schwenzer, S. P., Bridges, J. C., Banham, S., Wiens, R. C., Gasnault, O., et al. (2020). Geochemical variation in the Stimson formation of Gale crater: Provenance, mineral sorting, and a comparison with modern Martian dunes. *Icarus*, 341, 113622. <https://doi.org/10.1016/j.icarus.2020.113622>
- Bell, J. F., Morris, R. V., & Adams, J. B. (1993). Thermally altered palagonitic tephra: A spectral and process analog to the soil and dust of Mars. *Journal of Geophysical Research*, 98(E2), 3373–3385. <https://doi.org/10.1029/92JE02367>
- Berger, J. A., Gellert, R., Boyd, N. I., King, P. L., McCraig, M. A., O'Connell-Cooper, C. D., et al. (2020). Elemental composition and chemical evolution of geologic materials in Gale crater, Mars: APXS results from Bradbury landing to the Vera Rubin Ridge. *Journal of Geophysical Research: Planets*, 125(12), e2020JE006536. <https://doi.org/10.1029/2020JE006536>
- Bhattacharya, J. P., Payenberg, T. H. D., Lang, S. C., & Bourke, M. (2005). Dynamic river channels suggest a long-lived Noachian crater lake on Mars. *Geophysical Research Letters*, 32(10), 1–4. <https://doi.org/10.1029/2005GL022747>
- Bibring, J. P., Langevin, Y., Gendrin, A., Gondet, B., Poulet, F., Berthé, M., et al. (2005). Mars surface diversity as revealed by the OMEGA/Mars Express observations. *Science*, 307(5715), 1576–1581. <https://doi.org/10.1126/science.1108806>
- Bishop, J. L., Fairén, A. G., Michalski, J. R., Gago-Duport, L., Baker, L. L., Velbel, M. A., et al. (2018). Surface clay formation during short-term warmer and wetter conditions on a largely cold ancient Mars. *Nature Astronomy*, 2(3), 206–213. <https://doi.org/10.1038/s41550-017-0377-9>
- Bishop, J. L., Schiffman, P., & Southard, R. (2002). Geochemical and mineralogical analyses of palagonitic tuffs and altered rinds of pillow basalts in Iceland and applications to Mars. *Geological Society Special Publication*, 202, 371–392. <https://doi.org/10.1144/GSL.SP.2002.202.01.19>
- Boudier, F., & Nicolas, A. (2011). Axial melt lenses at oceanic ridges—A case study in the Oman ophiolite. *Earth and Planetary Science Letters*, 304(3–4), 313–325. <https://doi.org/10.1016/j.epsl.2011.01.029>
- Bowden, D. L., Bridges, J. C., Cousin, A., Rapin, W., Semprich, J., Gasnault, O., et al. (2023). Askival: An altered feldspathic cumulate sample in Gale crater. *Meteoritics & Planetary Sciences*, 58(1), 41–62. <https://doi.org/10.1111/MAPS.13933>
- Brož, P., Bernhardt, H., Conway, S. J., & Parekh, R. (2021). An overview of explosive volcanism on Mars. *Journal of Volcanology and Geothermal Research*, 409, 107125. <https://doi.org/10.1016/j.jvolgeores.2020.107125>
- Butcher, F. E. G., Balme, M. R., Gallagher, C., Arnold, N. S., Conway, S. J., Hagermann, A., & Lewis, S. R. (2017). Recent basal melting of a mid-latitude glacier on Mars. *Journal of Geophysical Research: Planets*, 122(12), 2445–2468. <https://doi.org/10.1002/2017JE005434>
- Butcher, F. E. G., Conway, S. J., & Arnold, N. S. (2016). Are the Dorsa Argentea on Mars eskers? *Icarus*, 275, 65–84. <https://doi.org/10.1016/j.icarus.2016.03.028>
- Byrne, S. (2009). The polar deposits of Mars. *Annual Review of Earth and Planetary Sciences*, 37(1), 535–560. <https://doi.org/10.1146/ANNUREV.EARTH.031208.100101/CITE/REFWORKS>
- Carr, M., & Head, J. (2019). Mars: Formation and fate of a frozen Hesperian ocean. *Icarus*, 319, 433–443. <https://doi.org/10.1016/j.icarus.2018.08.021>
- Carr, M. H., & Head, J. W. (2010). Geologic history of Mars. *Earth and Planetary Science Letters*, 294(3–4), 185–203. <https://doi.org/10.1016/j.epsl.2009.06.042>
- Carson, G. L., McHenry, L. J., Hynek, B. M., Cameron, B. I., & Glenister, C. T. (2023). Mineralogy and geochemistry of hot spring deposits at Námafjall, Iceland: Analog for sulfate soils at Gusev crater, Mars. *American Mineralogist*, 108(4), 637–652. <https://doi.org/10.2138/AM-2022-8364>
- Chapman, M. G. (1994). Evidence, age, and thickness of a frozen Paleolake in Utopia Planitia, Mars. *Icarus*, 109(2), 393–406. <https://doi.org/10.1006/ICAR.1994.1102>
- Chapman, M. G. (2003). Sub-ice volcanoes and ancient oceans/lakes: A Martian challenge. *Global and Planetary Change*, 35(3–4), 185–198. [https://doi.org/10.1016/S0921-8181\(02\)00126-1](https://doi.org/10.1016/S0921-8181(02)00126-1)
- Chapman, M. G., & Tanaka, K. L. (2001). Interior trough deposits on Mars: Subice volcanoes? *Journal of Geophysical Research*, 106(E5), 10087–10100. <https://doi.org/10.1029/2000JE001303>
- Chapman, M. G., & Tanaka, K. L. (2002). Related magma–ice interactions: Possible origins of chasmata, chaos, and surface materials in Xanthe, Margaritifer, and Meridiani Terrae, Mars. *Icarus*, 155(2), 324–339. <https://doi.org/10.1006/ICAR.2001.6735>
- Clifford, S. M., Crisp, D., Fisher, D. A., Herkenhoff, K. E., Smrekar, S. E., Thomas, P. C., et al. (2000). The state and future of Mars polar science and exploration. *Icarus*, 144(2), 210–242. <https://doi.org/10.1006/ICAR.1999.6290>
- Clifford, S. M., & Parker, T. J. (2001). The evolution of the Martian hydrosphere: Implications for the fate of a Primordial Ocean and the current state of the northern plains. *Icarus*, 154(1), 40–79. <https://doi.org/10.1006/ICAR.2001.6671>
- Cockell, C. S., Olsson, K., Knowles, F., Kelly, L., Herrera, A., Thorsteinnsson, T., & Marteinnsson, V. (2009). Bacteria in weathered basaltic glass, Iceland. *Geomicrobiology Journal*, 26(7), 491–507. <https://doi.org/10.1080/01490450903061101>
- Cornwall, C., Bandfield, J. L., Titus, T. N., Schreiber, B. C., & Montgomery, D. R. (2015). Physical abrasion of mafic minerals and basalt grains: Application to Martian Aeolian deposits. *Icarus*, 256, 13–21. <https://doi.org/10.1016/j.icarus.2015.04.020>
- Cousin, A., Sautter, V., Payré, V., Forni, O., Mangold, N., Gasnault, O., et al. (2017). Classification of igneous rocks analyzed by ChemCam at Gale crater, Mars. *Icarus*, 288, 265–283. <https://doi.org/10.1016/j.icarus.2017.01.014>
- Cousins, C. R. (2015). Volcanogenic fluvial-lacustrine environments in Iceland and their utility for identifying past habitability on Mars. *Life (Basel, Switzerland)*, 5(1), 568–586. <https://doi.org/10.3390/life5010568>
- Craddock, R. A., & Howard, A. D. (2002). The case for rainfall on a warm, wet early Mars. *Journal of Geophysical Research*, 107(11), 21–1–21–36. <https://doi.org/10.1029/2001JE001505>
- Craddock, R. A., & Maxwell, T. A. (1993). Geomorphic evolution of the Martian highlands through ancient fluvial processes. *Journal of Geophysical Research*, 98(E2), 3453–3468. <https://doi.org/10.1029/92JE02508>
- Daniel Steven Kelly, B. (2018). *Analysis of geological materials by low dilution fusion at the Peter Hooper geoanalytical lab (Washington State University)*. Washington State University. Retrieved from <https://rex.libraries.wsu.edu/esploro/outputs/99900525127101842>
- Davis, J. M., Balme, M., Grindrod, P. M., Williams, R. M. E., & Gupta, S. (2016). Extensive Noachian fluvial systems in Arabia Terra: Implications for early Martian climate. *Geology*, 44(10), 847–850. <https://doi.org/10.1130/G38247.1>
- Di Achille, G., & Hynek, B. M. (2010). Ancient ocean on Mars supported by global distribution of deltas and valleys. *Nature Geoscience*, 3(7), 459–463. <https://doi.org/10.1038/ngeo891>
- Dickson, J. L., Lamb, M. P., Williams, R. M. E., Hayden, A. T., & Fischer, W. W. (2021). The global distribution of depositional rivers on early Mars. *Geology*, 49(5), 504–509. <https://doi.org/10.1130/G48457.1>

- Doebelin, N., & Kleeberg, R. (2015). Profex: A graphical user interface for the Rietveld refinement program BGMN. *Journal of Applied Crystallography*, 48(5), 1573–1580. <https://doi.org/10.1107/S1600576715014685>
- Drief, A., & Schiffman, P. (2004). Very low-temperature alteration of sideromelane in hyaloclastites and hyalotuffs from Kilauea and Mauna Kea volcanoes: Implications for the mechanism of palagonite formation. *Clays and Clay Minerals*, 52(5), 622–634. <https://doi.org/10.1346/CCMN.2004.0520508>
- Eason, D. E., Sinton, J. M., Grönvold, K., & Kurz, M. D. (2015). Effects of deglaciation on the petrology and eruptive history of the Western Volcanic Zone, Iceland. *Bulletin of Volcanology*, 77(6), 1–27. <https://doi.org/10.1007/S00445-015-0916-0/FIGURES/10>
- Edwards, P. H., Bridges, J. C., Wiens, R., Anderson, R., Dyar, D., Fisk, M., et al. (2017). Basalt-trachybasalt samples in Gale crater, Mars. *Meteoritics & Planetary Sciences*, 52(11), <https://doi.org/10.1111/maps.12953>
- Ehlmann, B. L., & Edwards, C. S. (2014). Mineralogy of the Martian surface. *Annual Review of Earth and Planetary Sciences*, 42(1), 291–315. <https://doi.org/10.1146/ANNUREV-EARTH-060313-055024>
- Ehlmann, B. L., Mustard, J. F., Swayze, G. A., Clark, R. N., Bishop, J. L., Poulet, F., et al. (2009). Identification of hydrated silicate minerals on Mars using MRO-CRISM: Geologic context near Nili Fossae and implications for aqueous alteration. *Journal of Geophysical Research*, 114(E2), E00D08. <https://doi.org/10.1029/2009JE003339>
- Einarsson, P., Grönvold, K., Oskarsson, N., Einarsson, P., Grönvold, K., & Oskarsson, N. (2013). *Origin of macrocrysts and Gabbro Nodules in Hengill, SW Iceland* (pp. V31A–2679). AGUFM. Retrieved from <https://ui.adsabs.harvard.edu/abs/2013AGUFM.V31A2679E/abstract>
- Ewing, R. C., Rampe, E. B., Horgan, B. H. N., Lapotre, M. G. A., Nachon, M., Thorpe, M., et al. (2019). SAND-E: Semi-autonomous navigation for detrital environments first results. In *AGU fall meeting 2019*. AGU.
- Farley, K. A., Williford, K. H., Stack, K. M., Bhartia, R., Chen, A., de la Torre, M., et al. (2020). Mars 2020 mission overview. *Space Science Reviews*, 216(8), 1–41. <https://doi.org/10.1007/S11214-020-00762-Y/TABLES/1>
- Fassett, C. I., & Head, J. W. (2005). Fluvial sedimentary deposits on Mars: Ancient deltas in a crater lake in the Nili Fossae region. *Geophysical Research Letters*, 32(14), 1–5. <https://doi.org/10.1029/2005GL023456>
- Fawdon, P., Skok, J. R., Balme, M. R., Vye-Brown, C. L., Rothery, D. A., & Jordan, C. J. (2015). The geological history of Nili Patera, Mars. *Journal of Geophysical Research: Planets*, 120(5), 951–977. <https://doi.org/10.1002/2015JE004795>
- Feldman, W. C., Prettyman, T. H., Maurice, S., Plaut, J. J., Bish, D. L., Vaniman, D. T., et al. (2004). Global distribution of near-surface hydrogen on Mars. *Journal of Geophysical Research*, 109(E9), 9006. <https://doi.org/10.1029/2003JE002160>
- Filiberto, J., Baratoux, D., Beaty, D., Breuer, D., Farcy, B. J., Grott, M., et al. (2016). A review of volatiles in the Martian interior. *Meteoritics & Planetary Sciences*, 51(11), 1935–1958. <https://doi.org/10.1111/MAPS.12680>
- Gellert, R., Rieder, R., Brückner, J., Clark, B. C., Dreibus, G., Klingelhöfer, G., et al. (2006). Alpha particle X-ray spectrometer (APXS): Results from Gusev crater and calibration report. *Journal of Geophysical Research*, 111(E2), E02S05. <https://doi.org/10.1029/2005JE002555>
- Ghatan, G. J., & Head, J. W. (2002). Candidate subglacial volcanoes in the south polar region of Mars: Morphology, morphometry, and eruption conditions. *Journal of Geophysical Research*, 107(E7), 2-1–2-19. <https://doi.org/10.1029/2001JE001519>
- Grau Galofre, A., Whipple, K. X., Christensen, P. R., & Conway, S. J. (2022). Valley networks and the record of glaciation on ancient Mars. *Geophysical Research Letters*, 49(14), e2022GL097974. <https://doi.org/10.1029/2022GL097974>
- Grotzinger, J. P., Gupta, S., Malin, M. C., Rubin, D. M., Schieber, J., Siebach, K., et al. (2015). Deposition, exhumation, and paleoclimate of an ancient lake deposit, Gale crater, Mars. *Science*, 350(6257), aac7575. <https://doi.org/10.1126/science.aac7575>
- Grotzinger, J. P., Sumner, D. Y., Kah, L. C., Stack, K., Gupta, S., Edgar, L., et al. (2014). A habitable fluvio-lacustrine environment at Yellowknife Bay, Gale crater, Mars. *Science*, 343(6169), 1242777. <https://doi.org/10.1126/science.1242777>
- Gudmundsson, A. (1995). Infrastructure and mechanics of volcanic systems in Iceland. *Journal of Volcanology and Geothermal Research*, 64(1–2), 1–22. [https://doi.org/10.1016/0377-0273\(95\)92782-Q](https://doi.org/10.1016/0377-0273(95)92782-Q)
- Gudmundsson, M. T., Sigmundsson, F., & Björnsson, H. (1997). Ice–volcano interaction of the 1996 Gjalp subglacial eruption, Vatnajökull, Iceland. *Nature*, 389(6654), 954–957. <https://doi.org/10.1038/40122>
- Gurenko, A. A., & Sobolev, A. V. (2006). Crust-primitive magma interaction beneath neovolcanic rift zone of Iceland recorded in gabbro xenoliths from Midfell, SW Iceland. *Contributions to Mineralogy and Petrology*, 151(5), 495–520. <https://doi.org/10.1007/S00410-006-0079-2/METRICS>
- Head, J. W., & Wilson, L. (2007). Heat transfer in volcano–ice interactions on Mars: Synthesis of environments and implications for processes and landforms. *Annals of Glaciology*, 45, 1–13. <https://doi.org/10.3189/172756407782282570>
- Henderson, M. J. B., Horgan, B. H. N., Rowe, M. C., Wall, K. T., & Scudder, N. A. (2021). Determining the volcanic eruption style of tephra deposits from infrared spectroscopy. *Earth and Space Science*, 8(2), e2019EA001013. <https://doi.org/10.1029/2019EA001013>
- Hodges, C. A., & Moore, H. J. (1979). The subglacial birth of Olympus Mons and its aureoles. *Journal of Geophysical Research*, 84(B14), 8061–8074. <https://doi.org/10.1029/JB0841B14P08061>
- Honnorez, J., & Kirst, P. (1975). Submarine basaltic volcanism: Morphometric parameters for discriminating hyaloclastites from hyalotuffs. *Bulletin Volcanologique*, 39(3), 441–465. <https://doi.org/10.1007/BF02597266/METRICS>
- Horgan, B., & Bell, J. F. (2012). Widespread weathered glass on the surface of Mars. *Geology*, 40(5), 391–394. <https://doi.org/10.1130/G32755.1>
- Horgan, B. H. N., Anderson, R. B., Dromart, G., Amador, E. S., & Rice, M. S. (2020). The mineral diversity of Jezero crater: Evidence for possible lacustrine carbonates on Mars. *Icarus*, 339, 113526. <https://doi.org/10.1016/j.icarus.2019.113526>
- Horvath, D. G., Moitra, P., Hamilton, C. W., Craddock, R. A., & Andrews-Hanna, J. C. (2021). Evidence for geologically recent explosive volcanism in Elysium Planitia, Mars. *Icarus*, 365, 114499. <https://doi.org/10.1016/j.icarus.2021.114499>
- Höskuldsson, A., Sparks, R. S. J., & Carroll, M. R. (2006). Constraints on the dynamics of subglacial basalt eruptions from geological and geochemical observations at Kverkfjöll, NE-Iceland. *Bulletin of Volcanology*, 68(7–8), 689–701. <https://doi.org/10.1007/S00445-005-0043-4/FIGURES/13>
- Hovius, N., Lea-Cox, A., & Turowski, J. M. (2008). Recent volcano–ice interaction and outburst flooding in a Mars polar cap re-entrant. *Icarus*, 197(1), 24–38. <https://doi.org/10.1016/j.icarus.2008.04.020>
- Jakobsson, S. P., & Gudmundsson, M. T. (2008). Subglacial and intraglacial volcanic formations in Iceland. In *Jökull* (58th ed., pp. 179–196).
- Jakobsson, S. P., & Johnson, G. L. (2012). Intraglacial volcanism in the western volcanic zone, Iceland. *Bulletin of Volcanology*, 74(5), 1141–1160. <https://doi.org/10.1007/S00445-012-0589-X/FIGURES/11>
- Jakobsson, S. P., Jónsson, J., & Shido, F. (1978). Petrology of the western Reykjanes Peninsula, Iceland. *Journal of Petrology*, 19(4), 669–705. <https://doi.org/10.1093/PETROLOGY/19.4.669>
- Jakobsson, S. P., & Moore, J. G. (1986). Hydrothermal minerals and alteration rates at Surtsey volcano, Iceland. *GSA Bulletin*, 97(5), 648–659. [https://doi.org/10.1130/0016-7606\(1986\)97%3C648:HMAARA%3E2.0.CO;2](https://doi.org/10.1130/0016-7606(1986)97%3C648:HMAARA%3E2.0.CO;2)
- Jakosky, B. M., Henderson, B. G., & Mellon, M. T. (1995). Chaotic obliquity and the nature of the Martian climate. *Journal of Geophysical Research*, 100(E1), 1579–1584. <https://doi.org/10.1029/94JE02801>

- Johnson, D. M., Hooper, P. R., & Conrey, R. M. (1999). XRF analysis of rocks and minerals for major and trace elements on a single low dilution Li-tetraborate fused bead. *Advances in X-Ray Analysis*, 41, 843–867.
- Jull, M., & McKenzie, D. (1996). The effect of deglaciation on mantle melting beneath Iceland. *Journal of Geophysical Research: Solid Earth*, 101(B10), 21815–21828. <https://doi.org/10.1029/96jb01308>
- Kadish, S. J., Head, J. W., Parsons, R. L., & Marchant, D. R. (2008). The Ascræus Mons fan-shaped deposit: Volcano–ice interactions and the climatic implications of cold-based tropical mountain glaciation. *Icarus*, 197(1), 84–109. <https://doi.org/10.1016/J.ICARUS.2008.03.019>
- Kelly, L. C., Cockell, C. S., Piceno, Y. M., Andersen, G. L., Thorsteinsson, T., & Marteinsson, V. (2010). Bacterial diversity of weathered terrestrial Icelandic volcanic glasses. *Microbial Ecology*, 60(4), 740–752. <https://doi.org/10.1007/S00248-010-9684-8/FIGURES/6>
- Lapôtre, M. G. A., Bishop, J. L., Ielpi, A., Lowe, D. R., Siebach, K. L., Sleep, N. H., & Tikoo, S. M. (2022). Mars as a time machine to Precambrian Earth. *Journal of the Geological Society*, 179(5). <https://doi.org/10.1144/JGS2022-007>
- Le Masurier, W. E. (2002). Architecture and evolution of hydrovolcanic deltas in Marie Byrd Land, Antarctica. *Geological Society Special Publication*, 202(1), 115–148. <https://doi.org/10.1144/GSL.SP.2002.202.01.07>
- Leone, G. (2021). *Explosive volcanism on mars* (pp. 183–230). A Volcanic World. https://doi.org/10.1007/978-3-030-84103-4_8/FIGURES/3
- Levrard, B., Forget, F., Montmessin, F., & Laskar, J. (2004). Recent ice-rich deposits formed at high latitudes on Mars by sublimation of unstable equatorial ice during low obliquity. *Nature*, 431(7012), 1072–1075. <https://doi.org/10.1038/nature03055>
- Liu, E. J., Cashman, K. V., Rust, A. C., & Edmonds, M. (2018). Insights into the dynamics of mafic magmatic-hydromagmatic eruptions from volatile degassing behaviour: The Hverfjall Fires, Iceland. *Journal of Volcanology and Geothermal Research*, 358, 228–240. <https://doi.org/10.1016/J.JVOLGEORES.2018.05.016>
- Liu, Y., Tice, M. M., Schmidt, M. E., Treiman, A. H., Kizovski, T. V., Hurowitz, J. A., et al. (2022). An olivine cumulate outcrop on the floor of Jezero crater, Mars. *Science*, 377(6614), 1513–1519. https://doi.org/10.1126/SCIENCE.ABO2756/SUPPL_FILE/SCIENCE.ABO2756_MOVIE_S1.ZIP
- MacLennan, J., Jull, M., McKenzie, D., Slater, L., & Gronvold, K. (2002). The link between volcanism and deglaciation in Iceland. *Geochemistry, Geophysics, Geosystems*, 3(11), 1–25. <https://doi.org/10.1029/2001GC000282>
- Mangold, N., Baratoux, D., Arnalds, O., Bardintzeff, J.-M., Platevoet, B., Grégoire, M., & Pinet, P. (2011). Segregation of olivine grains in volcanic sands in Iceland and implications for Mars. *Earth and Planetary Science Letters*, 310(3–4), 233–243. <https://doi.org/10.1016/J.EPSL.2011.07.025>
- Martínez-Alonso, S., Mellon, M. T., Banks, M. E., Keszthelyi, L. P., & McEwen, A. S. (2011). Evidence of volcanic and glacial activity in Chryse and Acidalia Planitiae, Mars. *Icarus*, 212(2), 597–621. <https://doi.org/10.1016/J.ICARUS.2011.01.004>
- McGarvie, D. W., Stevenson, J. A., Burgess, R., Tuffen, H., & Tindle, A. G. (2007). Volcano–ice interactions at Prestahnúkur, Iceland: Rhyolite eruption during the last interglacial–glacial transition. *Annals of Glaciology*, 45, 38–47. <https://doi.org/10.3189/172756407782282453>
- McLennan, S. M., Grotzinger, J. P., Hurowitz, J. A., & Tosca, N. J. (2019). The sedimentary cycle on early Mars. *Annual Review of Earth and Planetary Sciences*, 47(1), 91–118. <https://doi.org/10.1146/ANNUREV-EARTH-053018-060332>
- Moitra, P., Horvath, D. G., & Andrews-Hanna, J. C. (2021). Investigating the roles of magmatic volatiles, ground ice and impact-triggering on a very recent and highly explosive volcanic eruption on Mars. *Earth and Planetary Science Letters*, 567, 116986. <https://doi.org/10.1016/J.EPSL.2021.116986>
- Morgan, A. M., Wilson, S. A., & Howard, A. D. (2022). The global distribution and morphologic characteristics of fan-shaped sedimentary landforms on Mars. *Icarus*, 385, 115137. <https://doi.org/10.1016/J.ICARUS.2022.115137>
- Morris, R. V., Vaniman, D. T., Blake, D. F., Gellert, R., Chipera, S. J., Rampe, E. B., et al. (2016). Silicic volcanism on Mars evidenced by tridymite in high-SiO₂ sedimentary rock at Gale crater. *Proceedings of the National Academy of Sciences of the United States of America*, 113(26), 7071–7076. https://doi.org/10.1073/PNAS.1607098113/SUPPL_FILE/PNAS.1607098113.SAPP.PDF
- Muirhead, B. K., Nicholas, A., & Umland, J. (2020). Mars sample return mission concept status. In *IEEE aerospace conference proceedings*. <https://doi.org/10.1109/AERO47225.2020.9172609>
- Mustard, J. F., Murchie, S. L., Pelkey, S. M., Ehlmann, B. L., Milliken, R. E., Grant, J. A., et al. (2008). Hydrated silicate minerals on Mars observed by the Mars Reconnaissance Orbiter CRISM instrument. *Nature*, 454(7202), 305–309. <https://doi.org/10.1038/nature07097>
- Németh, K., & Kósik, S. (2020). Review of explosive hydrovolcanism. *Geosciences*, 10(2), 44. <https://doi.org/10.3390/GEOSCIENCES10020044>
- Newsom, H. E., Brittelle, G. E., Hibbitts, C. A., Crossey, L. J., & Kudo, A. M. (1996). Impact crater lakes on Mars. *Journal of Geophysical Research*, 101(E6), 14951–14955. <https://doi.org/10.1029/96JE01139>
- Ori, G. G., Marinangeli, L., & Baliva, A. (2000). Terraces and Gilbert-type deltas in crater lakes in Ismenius Lacus and Memnonia (Mars). *Journal of Geophysical Research*, 105(E7), 17629–17641. <https://doi.org/10.1029/1999JE001219>
- Pandey, A., Rampe, E. B., Ming, D. W., Deng, Y., Bedford, C. C., & Schwab, P. (2023). Quantification of amorphous Si, Al, and Fe in palagonitic Mars analogs by chemical extraction and X-ray spectroscopy. *Icarus*, 392, 115362. <https://doi.org/10.1016/J.ICARUS.2022.115362>
- Parker, T. J., Gorsline, D. S., Saunders, R. S., Pieri, D. C., & Schneeberger, D. M. (1993). Coastal geomorphology of the Martian northern plains. *Journal of Geophysical Research*, 98(E6), 11061–11078. <https://doi.org/10.1029/93JE00618>
- Payré, V., Siebach, K. L., Dasgupta, R., Udry, A., Rampe, E. B., & Morrison, S. M. (2020). Constraining ancient magmatic evolution on Mars using crystal chemistry of detrital igneous minerals in the sedimentary Bradbury group, Gale crater, Mars. *Journal of Geophysical Research: Planets*, 125(8), e2020JE006467. <https://doi.org/10.1029/2020JE006467>
- Pedersen, G. B. M., & Grosse, P. (2014). Morphometry of subaerial shield volcanoes and glaciovolcanoes from Reykjanes Peninsula, Iceland: Effects of eruption environment. *Journal of Volcanology and Geothermal Research*, 282, 115–133. <https://doi.org/10.1016/J.JVOLGEORES.2014.06.008>
- Pedersen, G. B. M., Grosse, P., & Gudmundsson, M. T. (2020). Morphometry of glaciovolcanic edifices from Iceland: Types and evolution. *Geomorphology*, 370, 107334. <https://doi.org/10.1016/J.GEOMORPH.2020.107334>
- Pope, A., Willis, I. C., Pálsson, F., Arnold, N. S., Gareth Rees, W., Björnsson, H., & Grey, L. (2016). Elevation change, mass balance, dynamics and surging of Langjökull, Iceland from 1997 to 2007. *Journal of Glaciology*, 62(233), 497–511. <https://doi.org/10.1017/jog.2016.55>
- Rampe, E. B., Blake, D. F., Bristow, T. F., Ming, D. W., Vaniman, D. T., Morris, R. V., et al. (2020). Mineralogy and geochemistry of sedimentary rocks and eolian sediments in Gale crater, Mars: A review after six Earth years of exploration with Curiosity. *Geochemistry*, 80(2), 125605. <https://doi.org/10.1016/J.CHEMER.2020.125605>
- Ryan, C., Ryan, C. H., Schmidt, M. E., Osinski, G. R., & Massey, E. A. (2024). A global database of Mars-relevant hydrovolcanic environments on Earth with potential biosignature preservation. *Geosphere*, 20(2), 547–576. <https://doi.org/10.1130/GES02712.1>
- Sautter, V., Fabre, C., Forni, O., Toplis, M. J., Cousin, A., Ollila, A. M., et al. (2014). Igneous mineralogy at Bradbury Rise: The first ChemCam campaign at Gale crater. *Journal of Geophysical Research: Planets*, 119(1), 30–46. <https://doi.org/10.1002/2013JE004472>
- Scanlon, K. E., Head, J. W., Wilson, L., & Marchant, D. R. (2014). Volcano-ice interactions in the Arsia Mons tropical mountain glacier deposits. *Icarus*, 237, 315–339. <https://doi.org/10.1016/j.icarus.2014.04.024>

- Schon, S. C., Head, J. W., & Fassett, C. I. (2012). An overfilled lacustrine system and progradational delta in Jezero crater, Mars: Implications for Noachian climate. *Planetary and Space Science*, 67(1), 28–45. <https://doi.org/10.1016/j.pss.2012.02.003>
- Schuenemeyer, J., & Drew, L. (2011). Statistics for Earth and environmental scientists. Retrieved from <https://books.google.co.uk/books?hl=en&lr=&id=nqPgItP5MfYc&oi=fnd&pg=PR9&dq=Statistics+for+earth+and+environmental+scientists,&ots=jBey2kuBlr&sig=rYXxob7ZVvYvJvBr3Ldc934YHPW0>
- Siebach, K. L., Baker, M. B., Grotzinger, J. P., McLennan, S. M., Gellert, R., Thompson, L. M., & Hurowitz, J. A. (2017). Sorting out compositional trends in sedimentary rocks of the Bradbury group (Aeolis Palus), Gale crater, Mars. *Journal of Geophysical Research: Planets*, 122(2), 295–328. <https://doi.org/10.1002/2016JE005195>
- Sigmundsson, F., Pínel, V., Lund, B., Albino, F., Pagli, C., Geirsson, H., & Sturkell, E. (2010). Climate effects on volcanism: Influence on magmatic systems of loading and unloading from ice mass variations, with examples from Iceland. *Philosophical Transactions of the Royal Society A: Mathematical, Physical & Engineering Sciences*, 368(1919), 2519–2534. <https://doi.org/10.1098/RSTA.2010.0042>
- Sigvaldason, G. E. (1968). Structure and products of subaquatic volcanoes in Iceland. *Contributions to Mineralogy and Petrology*, 18(1), 1–16. <https://doi.org/10.1007/BF00371983/METRICS>
- Sigvaldason, G. E., Annertz, K., & Nilsson, M. (1992). Effect of glacier loading/deloading on volcanism: Postglacial volcanic production rate of the Dyngjufljöll area, central Iceland. *Bulletin of Volcanology*, 54(5), 385–392. <https://doi.org/10.1007/BF00312320>
- Sinton, J., Grönvold, K., & Sæmundsson, K. (2005). Postglacial eruptive history of the western volcanic zone, Iceland. *Geochemistry, Geophysics, Geosystems*, 6(12), 12009. <https://doi.org/10.1029/2005GC001021>
- Skilling, I. P. (2002). Basaltic pahoehoe lava-fed deltas: Large-scale characteristics, clast generation, emplacement processes and environmental discrimination. *Geological Society Special Publication*, 202(1), 91–113. <https://doi.org/10.1144/GSL.SP.2002.202.01.06>
- Skilling, I. P. (2009). Subglacial to emergent basaltic volcanism at Hlöðufell, south-west Iceland: A history of ice-confinement. *Journal of Volcanology and Geothermal Research*, 185(4), 276–289. <https://doi.org/10.1016/J.JVOLGEORES.2009.05.023>
- Skilling, I. P., White, J. D. L., & McPhie, J. (2002). Peperite: A review of magma–sediment mingling. *Journal of Volcanology and Geothermal Research*, 114(1–2), 1–17. [https://doi.org/10.1016/S0377-0273\(01\)00278-5](https://doi.org/10.1016/S0377-0273(01)00278-5)
- Smellie, J. L. (2008). Basaltic subglacial sheet-like sequences: Evidence for two types with different implications for the inferred thickness of associated ice. *Earth-Science Reviews*, 88(1–2), 60–88. <https://doi.org/10.1016/J.EARSCIREV.2008.01.004>
- Smellie, J. L. (2018). Glaciovolcanism: A 21st century proxy for palaeo-ice. In *Past glacial environments* (2nd ed., pp. 335–375). <https://doi.org/10.1016/B978-0-08-100524-8.00010-5>
- Smellie, J. L., Johnson, J. S., McIntosh, W. C., Esser, R., Gudmundsson, M. T., Hambrey, M. J., & de Vries, B. V. W. (2008). Six million years of glacial history recorded in volcanic lithofacies of the James Ross Island Volcanic Group, Antarctic Peninsula. *Palaeogeography, Palaeoclimatology, Palaeoecology*, 260(1–2), 122–148. <https://doi.org/10.1016/j.palaeo.2007.08.011>
- Smith, R. J., McLennan, S. M., Achilles, C. N., Dehouck, E., Horgan, B. H. N., Mangold, N., et al. (2021). X-ray amorphous components in sedimentary rocks of Gale crater, Mars: Evidence for ancient formation and long-lived aqueous activity. *Journal of Geophysical Research: Planets*, 126(3), e2020JE006782. <https://doi.org/10.1029/2020JE006782>
- Sotiriou, P., & Polat, A. (2020). Comparisons between tethyan anorthosite-bearing ophiolites and Archean anorthosite-bearing layered intrusions: Implications for Archean geodynamic processes. *Tectonics*, 39(8), e2020TC006096. <https://doi.org/10.1029/2020TC006096>
- Souness, C., & Hubbard, B. (2012). Mid-latitude glaciation on Mars. *Progress in Physical Geography*, 36(2), 238–261. https://doi.org/10.1177/0309133312436570/ASSET/IMAGES/LARGE/10.1177_0309133312436570-FIG11.JPEG
- Squyres, S. W., & Kasting, J. F. (1994). Early Mars: How warm and how wet? *Science*, 265(5173), 744–749. <https://doi.org/10.1126/science.265.5173.744>
- Stronck, N. A., & Schmincke, H. U. (2001). Evolution of palagonite: Crystallization, chemical changes, and element budget. *Geochemistry, Geophysics, Geosystems*, 2(7), 1017. <https://doi.org/10.1029/2000GC000102>
- Stronck, N. A., & Schmincke, H. U. (2002). Palagonite—A review. *International Journal of Earth Sciences*, 91(4), 680–697. <https://doi.org/10.1007/S00531-001-0238-7/METRICS>
- Thomson, B. J., Bridges, N. T., Milliken, R., Baldrige, A., Hook, S. J., Crowley, J. K., et al. (2011). Constraints on the origin and evolution of the layered mound in Gale crater, Mars using Mars Reconnaissance Orbiter data. *Icarus*, 214(2), 413–432. <https://doi.org/10.1016/J.ICARUS.2011.05.002>
- Thordarson, T., & Larsen, G. (2007). Volcanism in Iceland in historical time: Volcano types, eruption styles and eruptive history. *Journal of Geodynamics*, 43(1), 118–152. <https://doi.org/10.1016/J.JOG.2006.09.005>
- Thorpe, M. T., Hurowitz, J. A., & Siebach, K. L. (2021). Source-to-sink terrestrial analogs for the paleoenvironment of Gale crater, Mars. *Journal of Geophysical Research: Planets*, 126(2), e2020JE006530. <https://doi.org/10.1029/2020JE006530>
- Treiman, A. H., Bish, D. L., Vaniman, D. T., Chipera, S. J., Blake, D. F., Ming, D. W., et al. (2016). Mineralogy, provenance, and diagenesis of a potassic basaltic sandstone on Mars: CheMin X-ray diffraction of the Windjana sample (Kimberley area, Gale crater). *Journal of Geophysical Research: Planets*, 121(1), 75–106. <https://doi.org/10.1002/2015JE004932>
- Tronnes, R. G. (1990). Basaltic melt evolution of the Hengill Volcanic System, SW Iceland, and evidence for clinopyroxene assimilation in primitive tholeiitic magmas. *Journal of Geophysical Research*, 95(B10), 15893–15910. <https://doi.org/10.1029/JB095IB10P15893>
- Udry, A., Gazel, E., & McSween, H. Y. (2018). Formation of evolved rocks at Gale crater by crystal fractionation and implications for Mars crustal composition. *Journal of Geophysical Research: Planets*, 123(6), 1525–1540. <https://doi.org/10.1029/2018JE005602>
- Udry, A., Ostwald, A., Sautter, V., Cousin, A., Beyssac, O., Forni, O., et al. (2023). A Mars 2020 perseverance SuperCam perspective on the igneous nature of the Máaz Formation at Jezero crater and link with Séítah, Mars. *Journal of Geophysical Research: Planets*, 128(7), e2022JE007440. <https://doi.org/10.1029/2022JE007440>
- van Otterloo, J., Cas, R. A. F., & Scutter, C. R. (2015). The fracture behaviour of volcanic glass and relevance to quench fragmentation during formation of hyaloclastite and phreatomagmatism. *Earth-Science Reviews*, 151, 79–116. <https://doi.org/10.1016/J.EARSCIREV.2015.10.003>
- Vink, G. E. (1984). A hotspot model for Iceland and the Vøring Plateau. *Journal of Geophysical Research*, 89(B12), 9949–9959. <https://doi.org/10.1029/JB089B12P09949>
- Wall, K. T., Rowe, M. C., Ellis, B. S., Schmidt, M. E., & Eccles, J. D. (2014). Determining volcanic eruption styles on Earth and Mars from crystallinity measurements. *Nature Communications*, 5(1), 1–8. <https://doi.org/10.1038/ncomms6090>
- Warner, N., Gupta, S., Lin, S. Y., Kim, J. R., Muller, J. P., & Morley, J. (2010). Late Noachian to Hesperian climate change on Mars: Evidence of episodic warming from transient crater lakes near Ares Vallis. *Journal of Geophysical Research*, 115(E6), 6013. <https://doi.org/10.1029/2009JE003522>
- Warner, N. H., & Farmer, J. D. (2010). Subglacial hydrothermal alteration minerals in Jökulhlaup deposits of southern Iceland, with implications for detecting past or present habitable environments on Mars. *Astrobiology*, 10(5), 523–547. <https://Home.Liebertpub.Com/Ast>. <https://doi.org/10.1089/AST.2009.0425>

- Weisenberger, T., & Selbekk, R. S. (2009). Multi-stage zeolite facies mineralization in the Hvalfjörður area, Iceland. *International Journal of Earth Sciences*, 98(5), 985–999. <https://doi.org/10.1007/S00531-007-0296-6>FIGURES/10
- Weitz, C. M., Milliken, R. E., Grant, J. A., McEwen, A. S., Williams, R. M. E., & Bishop, J. L. (2008). Light-toned strata and inverted channels adjacent to Juventae and Ganges chasmata, Mars. *Geophysical Research Letters*, 35(19), L19202. <https://doi.org/10.1029/2008GL035317>
- White, J. D. L., & Houghton, B. F. (2006). Primary volcaniclastic rocks. *Geology*, 34(8), 677–680. <https://doi.org/10.1130/G22346.1>
- White, J. D. L. (2000). Subaqueous eruption-fed density currents and their deposits. *Precambrian Research*, 101(2–4), 87–109. [https://doi.org/10.1016/S0301-9268\(99\)00096-0](https://doi.org/10.1016/S0301-9268(99)00096-0)
- White, J. D. L., McPhie, J., & Soule, S. A. (2015). Submarine lavas and hyaloclastite. *The Encyclopedia of Volcanoes*, 363–375. <https://doi.org/10.1016/B978-0-12-385938-9.00019-5>
- Wood, D. A., Gibson, I. L., & Thompson, R. N. (1976). Elemental mobility during zeolite facies metamorphism of the Tertiary basalts of eastern Iceland. *Contributions to Mineralogy and Petrology*, 55(3), 241–254. <https://doi.org/10.1007/BF00371335>METRICS
- Wordsworth, R., Knoll, A. H., Hurowitz, J., Baum, M., Ehlmann, B. L., Head, J. W., & Steakley, K. (2021). A coupled model of episodic warming, oxidation and geochemical transitions on early Mars. *Nature Geoscience*, 14(3), 127–132. <https://doi.org/10.1038/s41561-021-00701-8>
- Xiao, L., Huang, J., Kusky, T., Head, J. W., Zhao, J., Wang, J., et al. (2023). Evidence for marine sedimentary rocks in Utopia Planitia: Zhurong rover observations. *National Science Review*, 10(9). <https://doi.org/10.1093/NSR/NWAD137>
- Zimanowski, B., & Buttner, R. (2003). Phreatomagmatic explosions in subaqueous volcanism. *Geophysical Monograph Series*, 140, 51–60. <https://doi.org/10.1029/140GM03>